Information & Functional Materials

WILEY

REVIEW OPEN ACCESS

Wide-Bandgap Semiconductor-Based Neuromorphic Computing

Hongyu Tang[1,2,3] | Pengsheng Min[1] | Yang Zhang[1] | Qingchun Zhang[1] | Wanlu Zhang[1] | Ruiqian Guo[1] | Guoqi Zhang[4]

[1]College of Intelligent Robotics and Advanced Manufacturing, Fudan University, Shanghai, China | [2]Shanghai Engineering Technology Research Center for SiC Power Device, Fudan University, Shanghai, China | [3]State Key Laboratory of Widegap Semiconductor Optoelectronic Materials and Technologies, Beijing, China | [4]EEMCS Faculty, Delft University of Technology, Delft, the Netherlands

Correspondence: Hongyu Tang (hongyu_tang@fudan.edu.cn) | Ruiqian Guo (rqguo@fudan.edu.cn)

Received: 23 January 2026 | **Revised:** 6 May 2026 | **Accepted:** 13 May 2026

Keywords: memristor | neuromorphic computing | synaptic transistor | wide-bandgap semiconductors (WBGSs)

ABSTRACT

Neuromorphic computing has emerged as a promising paradigm to overcome the energy inefficiency and data-transfer bottlenecks of conventional von Neumann architectures by emulating the parallel and adaptive information processing of biological neural systems. To date, most neuromorphic hardware has relied on silicon-compatible or narrow-bandgap materials, which often face intrinsic trade-offs among operating voltage, thermal stability, endurance, and multifunctionality. Wide-bandgap semiconductors (WBGSs)—including Group III nitrides, gallium oxide, silicon carbide, and diamond—provide an alternative material platform enabled by their large bandgaps, strong polarization effects, diverse defect states, and compatibility with electronic and optoelectronic device architectures. This review surveys recent progress in WBGS-based neuromorphic computing, with an emphasis on material-enabled device physics rather than isolated demonstrations. Typical device concepts, including memristors, synaptic transistors, and neuronal devices, are systematically discussed together with their underlying resistive switching, charge trapping, polarization modulation, and optoelectronic mechanisms. Strategies for device integration and performance benchmarking are also addressed. Finally, remaining challenges and future research directions toward scalable and energy-efficient neuromorphic systems based on WBGSs are outlined.

1 | Introduction

The rapid expansion of artificial intelligence has exposed fundamental limitations of conventional von Neumann computing architectures, particularly with respect to energy efficiency and data movement between separated memory and processing units. This data movement overhead primarily stems from the physical separation between memory and processing units, commonly referred to as the memory wall, a critical bottleneck where data frequently needs to be transferred back and forth between these two discrete components, resulting in substantial time latency and excessive energy consumption inherent in the conventional von Neumann framework. Neuromorphic computing, inspired by the brain's massively parallel and event-driven information processing, has therefore emerged as a promising alternative paradigm [1]. Hardware neuromorphic systems rely on electronic devices capable of emulating synaptic plasticity and neuronal dynamics, which has stimulated extensive research into novel material and device concepts. To date, most neuromorphic hardware demonstrations have been based on silicon (Si)-compatible technologies or narrow-bandgap semiconductors. However, these material platforms often suffer from trade-offs among endurance, retention, operating voltage, thermal stability, and environmental robustness, limiting their applicability in demanding operating conditions. This has motivated the explo-

ration of alternative material systems that can intrinsically support stable, efficient, and multifunctional neuromorphic behavior.

Wide-bandgap semiconductors (WBGSs), typically defined by bandgaps larger than ~2.5–3.0 eV, are well established in power electronics and optoelectronics owing to their high breakdown fields, large optical phonon energies, and excellent chemical and thermal stability. These intrinsic attributes also suggest compelling advantages for neuromorphic computing, particularly for devices operating at high speed, high power density, or under harsh environments. Importantly, WBGSs exhibit rich defect landscapes, strong polarization effects, and versatile interface properties, which can be deliberately exploited to realize analog resistive switching (RS), tunable conductance modulation, and diverse forms of synaptic plasticity.

As the fundamental building blocks of neuromorphic hardware, the performance of synaptic and neuronal devices is governed by the physicochemical properties of their constituent materials. Conventional neuromorphic devices are predominantly based on transition-metal oxides, organic materials, or two-dimensional materials (2DMs) [1, 2]. However, these systems are often vulnerable to performance degradation under extreme conditions such as high temperature or intense radiation, limiting their use in aerospace, nuclear, and other specialized applications. In contrast, WBGSs offer a distinctive combination of ultralow leakage current, high electron mobility (10^2–10^3 $cm^2 \cdot V^{-1}$ s^{-1}), excellent thermal conductivity (up to ~400 $W \cdot m^{-1}$ K^{-1}), and superior thermal and radiation stability. In addition, their favorable compatibility with established CMOS processes enables scalable fabrication and system-level integration. Currently, WBGSs explored for neuromorphic computing mainly include Group III nitrides (gallium nitride (GaN), aluminum nitride (AlN), and boron nitride (BN)), gallium oxide (Ga_2O_3), silicon carbide (SiC), and diamond. These materials exhibit unique advantages in synaptic weight (SW) modulation, low-power operation, and extreme-environment adaptability, collectively establishing WBGSs as a promising material platform for the diversified development of neuromorphic computing.

In this review, we focus on neuromorphic computing enabled by several aforementioned representative WBGSs, with particular emphasis on the correlations among material properties, device architectures, physical mechanisms, and system-level functionalities (Figure 1). Section 2 introduces key WBGS systems and their properties relevant to neuromorphic functions. Section 3 reviews representative neuromorphic device concepts based on WBGSs. Section 4 discusses the physical mechanisms underlying synaptic and neuronal behaviors. Section 5 addresses integration strategies, benchmarking metrics, and emerging application scenarios. Finally, Section 6 outlines the remaining challenges and future perspectives for WBGS-based neuromorphic computing.

2 | Wide-Bandgap Semiconductors for Neuromorphic Devices

2.1 | III–V Nitrides: GaN, BN, and AlN

Group III nitride WBGSs are characterized by strong spontaneous and piezoelectric polarization, high electron mobility, and

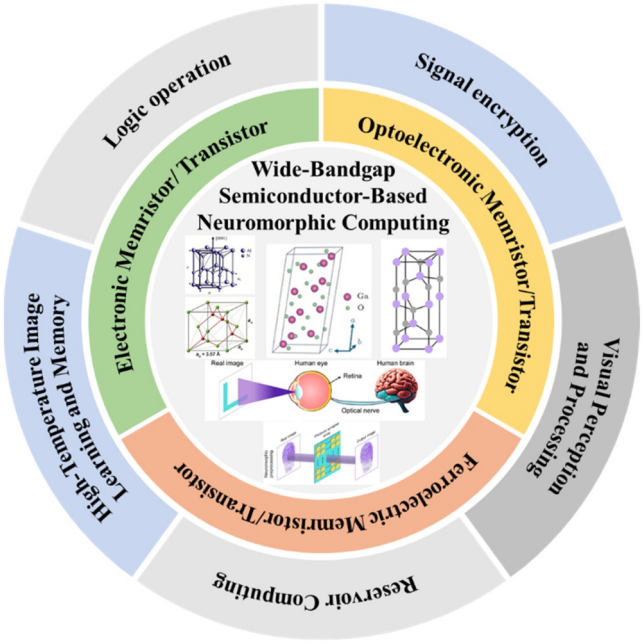

FIGURE 1 | Overview of wide-bandgap semiconductor-based neuromorphic computing. Reproduced with permission [3]. Copyright 2025, Journal of Materials Science. Reproduced with permission [4]. Copyright 2019, Materials Today Physics. Reproduced with permission [5]. Copyright 2025, Journal of Materials Research and Technology. Reproduced with permission [6]. Copyright 2025, Advanced Materials. Reproduced with permission [7]. Copyright 2024, Carbon-Based Nanofillers and Their Rubber Nanocomposites.

mature epitaxial growth technologies, making them a cornerstone of wide-bandgap semiconductor research. GaN, AlN, and BN are three representative III–V nitrides that have been extensively investigated for high-power electronics and deep-ultraviolet (DUV) optoelectronic applications. Beyond these conventional roles, their unique electronic structures, polarization effects, and interface properties provide a fertile platform for polarization-controlled synaptic transistors, memristive interfaces, and optoelectronic neuromorphic devices.

As a core material of third-generation semiconductor technologies, GaN exhibits a wide bandgap of ~3.4 eV, high thermal conductivity, and excellent resistance to high temperature, radiation, and chemical corrosion, collectively supporting stable device operation under extreme conditions and establishing GaN as a promising candidate for memristive devices [8]. Moreover, its hexagonal wurtzite crystal structure endows GaN with superior optoelectronic properties, enabling direct coupling between electrical and optical stimuli for visual neuromorphic systems [9]. As illustrated in Figure 2a, wurtzite GaN is a noncentrosymmetric single-crystal material with a well-defined polar axis (*c*-axis), along which strong spontaneous polarization and anisotropic piezoelectric coupling are present. This spontaneous polarization arises from the relative displacement between the charge centers of Ga^{3+} cations and N^{3-} anions, caused by the noncentrosymmetric stacking of Ga and N atomic planes along the polar axis. The [0001] crystallographic direction corresponds to Ga-polar surfaces, whereas the $[000\bar{1}]$ direction corresponds to N-polar surfaces, leading to polarity-dependent electronic and interfacial behaviors [12].

AlN exists in both wurtzite and zinc blende crystal structures, with the thermodynamically stable phase under ambient conditions being the wurtzite structure, characterized by lattice constants of $a = 3.112$ Å and $c = 4.982$ Å, as shown in Figure 2b [13]. Similar to GaN, wurtzite AlN exhibits strong spontaneous polarization along the *c*-axis due to the relative displacement of Al and N sublattices, resulting in two opposite polarization states associated with Al-polar and N-polar orientations. However, direct switching between these polarization states requires electric fields exceeding the dielectric breakdown strength, rendering conventional ferroelectric domain switching inaccessible. In strained AlGaN alloys, lattice distortion along the *c*-axis induces additional atomic displacement, giving rise to pronounced piezoelectric polarization effects that further modulate internal electric fields [14]. Notably, scandium (Sc) doping in AlN introduces substantial lattice deformation, manifested as a reduced c/a ratio and an increased metal-nitrogen bond parameter u along the *c*-axis [15]. With increasing Sc concentration, the crystal structure evolves from the stable wurtzite phase toward a metastable layered hexagonal structure characteristic of ScN. Although this layered hexagonal phase is intrinsically nonpolar, it represents an intermediate structural state between two oppositely polarized wurtzite configurations. Under this condition, external electric fields can induce polarization switching in AlScN ferroelectric thin films, enabling RS behavior.

BN represents a distinct class of III–V nitrides as a two-dimensional wide-bandgap material. In contrast to graphene, BN exhibits excellent insulating properties, ultralow dielectric loss, and exceptionally high thermal conductivity exceeding 750 $W \cdot m^{-1} K^{-1}$ [16, 17]. These attributes have enabled high-performance ultraviolet photodetectors with responsivities exceeding 10^5 A/W, ultralow-k dielectrics for sub-5-nm interconnect technologies, and resistive memory devices with endurance up to 10^8 cycles [18–20]. Among various BN polymorphs, hexagonal boron nitride (h-BN) is the most widely studied, featuring a layered structure analogous to graphite with atomically smooth interfaces and excellent chemical stability [17]. As shown in Figure 2c, its two-dimensional (2D) crystal structure and wide bandgap facilitate charge trapping and tunneling modulation, enabling memristive behavior and lossless integration of ultrathin, high-performance neuromorphic devices.

Overall, Groups III–V nitride WBGSs integrate multiple advantageous properties, including wide bandgaps ranging from ~3.4 to 6.2 eV, high thermal conductivity, high electron mobility, and exceptional chemical, thermal, and radiation stability, as listed in Table 1. Compared with conventional oxide materials, nitride semiconductors offer distinct advantages such as reduced phase randomness, strong and tunable polarization effects, and superior compatibility with established semiconductor processes. These characteristics help suppress thermally induced fluctuations and random filament formation during RS, thereby improving device uniformity and computational accuracy. Furthermore, the intrinsic coupling between spontaneous polarization and piezoelectric effects provides new degrees of freedom for regulating ion migration pathways, opening promising avenues for low-power, nonvolatile neuromorphic devices. Combined with their relatively low defect density, tunable trap states, and compatibility with Si substrates, III–V nitrides offer a robust and scalable material platform for high-performance neuromorphic computing.

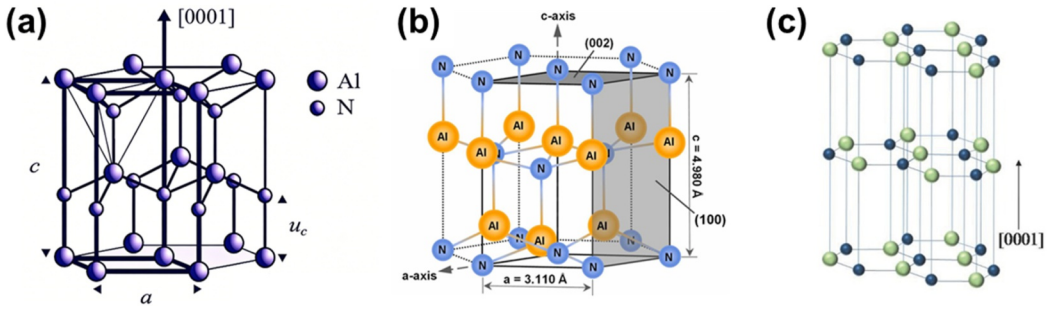

FIGURE 2 | Crystal structures. (a) GaN. Reproduced with permission [3]. Copyright 2025, Journal of Materials Science. (b) AlN. Reproduced with permission [10]. Copyright 2024, Journal of Alloys and Compounds. (c) BN. Reproduced with permission [11]. Copyright 2017, Advanced Electronic Materials.

TABLE 1 | A comparative discussion of bandgap, thermal conductivity, breakdown field, relative permittivity, and mobility [22, 23, 30–34].

Properties	Unit	GaN	AlN	h-BN	4H-SiC	6H-SiC	3C-SiC	β-Ga_2O_3	Diamond
Bandgap	eV	3.4	6.2	5.8	3.26	3.00	2.20	4.2–4.9	5.5
Thermal conductivity	W/cm·k	1.1	3.2	3.9	3	2.4	1.2	0.23[010] 0.13[100]	10
Breakdown field	MV/cm	3.3	2	7	4.9	4.9	4.9	8	10
Relative permittivity	—	9	8.5	6.85 (in-plane) 5.06 (out-of plane)	9.66	9.66	9.72	10	5.5
Mobility	cm^2/Vs	1200	135	35	800	400	900	300	2000

Note: — represents not reported.

2.2 | Silicon Carbide (SiC)

SiC is a representative WBGS that has attracted sustained interest due to its close structural and technological compatibility with silicon-based electronics. As a binary compound composed of silicon and carbon in a 1:1 atomic ratio, SiC exhibits more than 200 polymorphic and heteromorphic crystal configurations. Among these, 3C-, 4H-, and 6H-SiC are the most technologically relevant polytypes (Figure 3) [21]. In particular, 4H-SiC has emerged as a preferred material for neuromorphic device fabrication owing to its high electron mobility (~1000 $cm^2 \cdot V^{-1}\ s^{-1}$), wide bandgap (3.2–3.4 eV), and excellent thermal stability, with a melting point approaching 2700°C. SiC also exhibits a thermal conductivity approximately 3.3 times higher than that of conventional Si, enabling efficient heat dissipation and stable operation under high power density. Furthermore, its favorable tunability for both n-type and p-type doping provides flexibility in device design. The recent availability of commercial 8-inch 4H-SiC wafers represents a major milestone, laying a solid foundation for the large-scale integration and manufacturing of SiC-based neuromorphic circuits. SiC devices can operate reliably at temperatures up to ~550°C and exhibit superior resistance to ionizing radiation, making them highly suitable for neuromorphic computing in harsh environments. From a device-physics perspective, SiC offers additional advantages for neuromorphic applications. A high-quality SiO_2 layer can be readily grown on the SiC surface, providing effective oxidation protection and enabling well-controlled interfaces. Both intrinsic and extrinsic defects in SiC, including vacancies and interface traps, can act as charge trapping centers, facilitating nonvolatile and analog RS behaviors. These characteristics enable the realization of synaptic plasticity and stable weight modulation, positioning SiC as a robust material platform for high-temperature and radiation-hardened neuromorphic systems.

2.3 | Gallium Oxide (Ga_2O_3)

Ga_2O_3 is a typical ultrawide-bandgap semiconductor (UWBGS), featuring a bandgap energy ranging from ~4.6 to 4.9 eV and existing in six distinct crystalline phases (α, β, γ, δ, ε, and κ) [22], as shown in Figure 4. Among them, β-Ga_2O_3 has been most extensively studied due to its superior thermodynamic stability and relatively mature fabrication technologies. Ga_2O_3 is characterized by an exceptionally high breakdown electric field (~8 $MV \cdot cm^{-1}$), excellent chemical stability, and optical transparency, making it attractive for high-power and optoelectronic applications (Table 1). Thin films of Ga_2O_3 can be deposited using a variety of techniques, including magnetron sputtering and atomic layer deposition, and exhibit good compatibility with flexible substrates. As an emerging UWBGS, Ga_2O_3 has demonstrated broad application potential in power electronics, including resistive random-access memory (RRAM), Schottky barrier diodes, field-effect transistors, solar-blind photodetectors, radiation detectors, and DUV optoelectronic devices [23]. Ga_2O_3 exhibits annealing-temperature-dependent phase transitions and structural evolution, which provide additional degrees of freedom for tailoring its electronic and RS behaviors. In neuromorphic applications, Ga_2O_3-based memristors have demonstrated fast switching speeds, long data retention, and excellent endurance, enabling low-energy, multilevel, and scalable synaptic devices compatible with complementary metal-oxide-semiconductor (CMOS) processes and three-dimensional (3D) architectures [24]. Moreover, Ga_2O_3 exhibits a strong ultraviolet photoresponse arising from oxygen-vacancy-related defect states, enabling photoelectric synergistic modulation of SW. These characteristics make Ga_2O_3 particularly attractive for optoelectronic neuromorphic systems and visual bionic applications [4]. Although its ultrahigh breakdown field and defect-rich physics provide clear advantages for memristive neuromorphic devices, challenges related to thermal conductivity and heat dissipation remain and must be addressed for high-density integration.

2.4 | Diamond

Diamond represents a unique class of UWBGSs, combining an exceptionally wide bandgap with ultralow electronic noise, which enables highly sensitive detection of optical signals [25]. This characteristic is particularly advantageous for neuromorphic

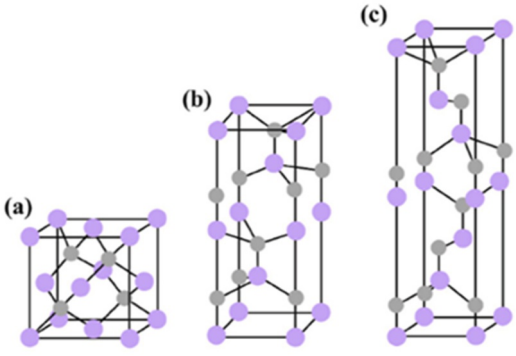

FIGURE 3 | Crystal structures of (a) 3C-, (b) 4H-, and (c) 6H-SiC polytypes. Reproduced with permission [5]. Copyright 2025, Journal of Materials Research and Technology.

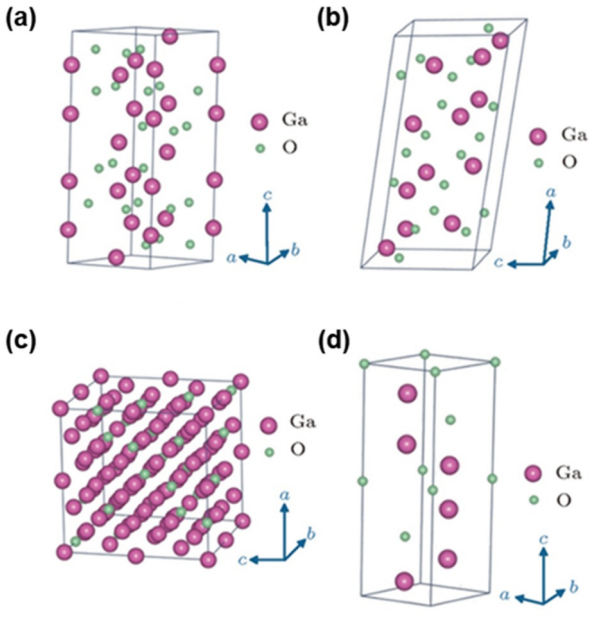

FIGURE 4 | Crystal structures of (a) α-, (b) β-, (c) γ-, and (d) ε-Ga_2O_3. Reproduced with permission [4]. Copyright 2019, Materials Today Physics.

photonic systems, where enhanced wavelength sensitivity and image recognition accuracy are required [26]. Additionally, diamond exhibits extreme hardness, outstanding chemical stability, and strong radiation resistance, ensuring long device lifetimes and reliable operation under harsh environmental conditions (Figure 5) [27]. Its ultrahigh thermal conductivity further supports stable device performance at elevated temperatures, making diamond an attractive candidate for neuromorphic applications in extreme environments [28]. Despite these advantages, diamond-based neuromorphic devices face notable limitations. First, their intrinsic photoresponse is primarily confined to the DUV region, which does not match the spectral sensitivity of biological vision systems. Second, the volatile nature of diamond photocurrents poses challenges for optical information storage and nonvolatile neuromorphic functions. Recent studies have shown that these limitations can be mitigated through interface engineering, particularly by exploiting hybrid diamond/graphene heterostructures. At the diamond/graphene interface, intermediate carbon bonding configurations (sp^3–sp^2) can reversibly transition between insulating and conductive states under external stimuli such as electric fields or optical excitation. This dynamic interfacial modulation gives rise to tunable resistance states and photoinduced conductivity, enabling the emulation of synaptic plasticity and neuronal behaviors [29]. Overall, diamond and related ultrawide-bandgap materials offer compelling opportunities for neuromorphic computing in extreme environments and photonic systems. Continued progress in interface engineering, defect modulation, and heterogeneous integration is expected to further unlock their potential for robust and multifunctional neuromorphic devices.

3 | Device Architectures for WBG Neuromorphic Computing

3.1 | Performance Parameters

3.1.1 | *Memristor*

As the fundamental building blocks of neuromorphic computing and next-generation nonvolatile memory systems, the practical performance of memristors is governed by a set of interrelated parameters that are intrinsically determined by their underlying RS mechanisms. Most memristors adopt a metal-insulator-metal (MIM) sandwich structure, within which RS behavior arises from electrically induced physical or chemical changes in the active layer or at the electrode interfaces [30].

Based on their dominant switching physics, memristors can be classified into three principal categories [24]: electrochemical metallization (ECM), valence change mechanism (VCM), and thermochemical mechanism (TCM), as schematically illustrated in Figure 6. In memristive operation, the SET process corresponds to the transition from a high-resistance state (HRS) to a low-resistance state (LRS), whereas the RESET process restores the device from the LRS to the HRS. In conductive-filament-based ECM and VCM devices, an external electric field drives the migration of metal cations or oxygen vacancies, leading to the formation of conductive filaments during the SET process, whereas reverse bias or Joule heating induces filament rupture during RESET. In contrast, redox-based or interface-type memristors rely on oxidation-reduction reactions at the electrode/active-layer interface, where modulation of the Schottky barrier height governs the resistance state. These distinct switching mechanisms directly dictate the achievable performance metrics of memristive devices.

Reliable RS with clearly distinguishable HRS and LRS, typically characterized by an on/off ratio exceeding 10^2 for practical applications, forms the foundation for effective information storage and signal encoding [31, 32]. For neuromorphic computing, gradual and controllable conductance modulation is essential to emulate SW updates. Such analog switching behavior is closely linked to the controllability of ion migration, defect redistribution, or charge trapping dynamics inherent to the RS mechanism. Energy efficiency is another critical parameter, particularly for large-scale crossbar arrays, where the target energy consumption per synaptic event ideally approaches the femtojoule (fJ) level comparable to biological synapses. This energy cost is fundamentally determined by the activation energy required for conductive-filament formation/rupture or interfacial redox reactions. Fast switching speed, spanning from subnanosecond to microsecond regimes, is necessary for high-throughput information processing and depends on the migration kinetics of ions or charge carriers in the active layer. Long-term reliability, reflected by high endurance (exceeding 10^9 switching cycles) and robust data retention (over 10 years at room temperature or stable operation at elevated temperatures), is particularly critical for WBGS-based devices intended for harsh environments and is

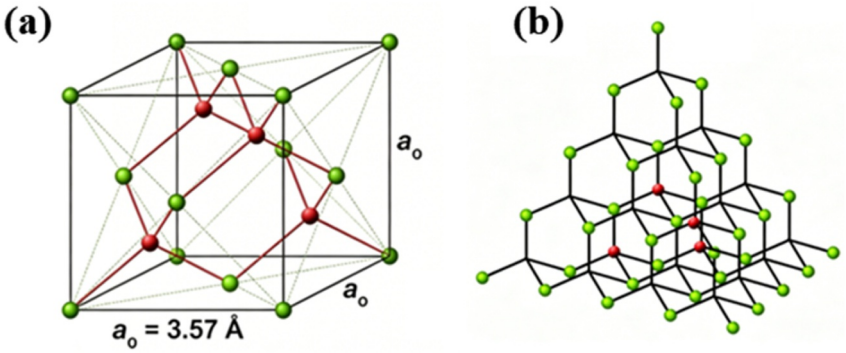

FIGURE 5 | Structure of diamond. (a) Unit-cell structure. (b) 3D structure. Reproduced with permission [7]. Copyright 2024, Carbon-Based Nanofillers and Their Rubber Nanocomposites.

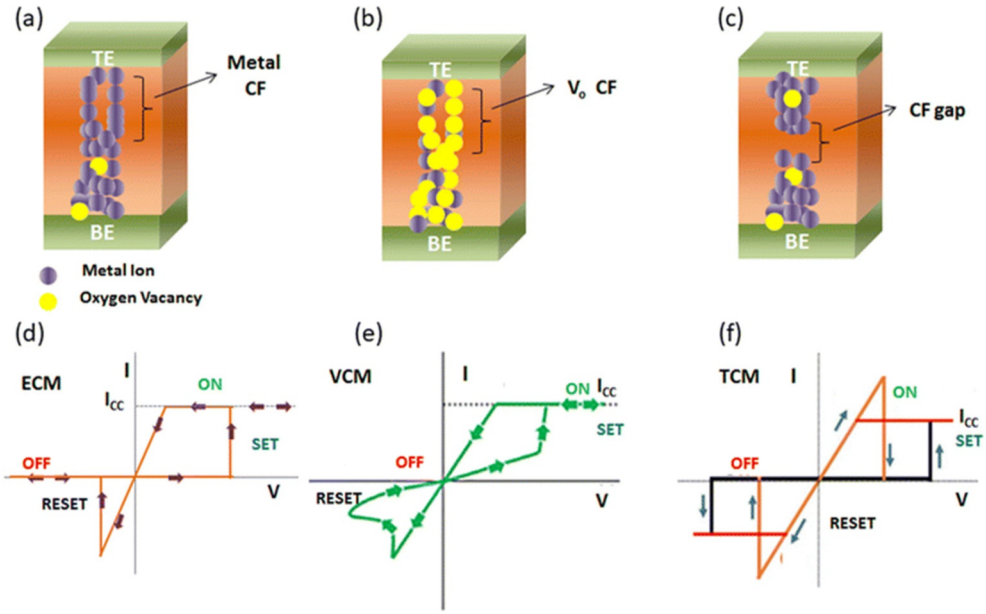

FIGURE 6 | Schematic illustrations of RS mechanisms. (a) ECM, (b) VCM, and (c) TCM. Representative hysteretic current-voltage (I–V) characteristics for (d) ECM, (e) VCM, and (f) TCM devices. Reproduced with permission [24]. Copyright 2025, Nanoscale.

governed by the structural stability of conductive paths and the reversibility of the switching processes.

Additionally, device-to-device and cycle-to-cycle uniformities are prerequisites for high-precision neuromorphic computation, as variability directly translates into computational noise in large-scale arrays. Uniformity is strongly influenced by the homogeneity of the active material, interface quality, and the degree of control over the RS mechanism. Consequently, optimizing memristor performance requires coordinated material engineering strategies—such as defect modulation, doping, heterostructure design, and interface engineering—to precisely regulate the dominant switching mechanisms. Continued advances along these directions are essential for translating memristor-based neuromorphic devices from laboratory demonstrations toward scalable, reliable, and commercially viable technologies.

3.1.2 | *Synaptic Devices*

The nervous system of organisms consists of a vast number of neurons interconnected by synapses, where presynaptic and postsynaptic neurons communicate through synaptic structures to facilitate the conduction of nerve impulses between neurons [33]. Synaptic connections are primarily categorized into two types: chemical synapses and electrical synapses [34]. Chemical synapses dominate in mammals, with signal transmission mediated by neurotransmitters, whereas electrical synapses rely on direct electrical signal conduction and are more prevalent in fish and amphibians. As schematically illustrated in Figure 7, a chemical synapse comprises three core structural components: the presynaptic terminal (axon terminal of the presynaptic neuron), the synaptic cleft, and the postsynaptic terminal (dendrite or cell body of the postsynaptic neuron) [37]. Upon the arrival of an action potential at the presynaptic terminal, membrane depolarization induces calcium ion influx through voltage-gated channels, triggering the release of neurotransmitters into the synaptic cleft [38]. These neurotransmitters bind to receptors on the postsynaptic membrane, modulating ion channel activity and generating postsynaptic currents or potentials [39]. Depending on the neurotransmitter type and receptor response, synaptic transmission can be excitatory or inhibitory, producing excitatory postsynaptic currents/potentials (EPSC/EPSP) or inhibitory postsynaptic currents/potentials (IPSC/IPSP) [40, 41]. These two complementary modes jointly regulate neural signal propagation and information processing. Artificial synaptic transistors aim to replicate these fundamental behaviors by mapping SW to channel conductance and using gate stimuli to emulate presynaptic spikes.

SW quantifies the strength of neuronal connections, whereas synaptic plasticity describes the adaptive modulation of SW in response to stimuli [42]. Artificial synaptic transistors can emulate essential plasticity characteristics of biological synapses, including short-term plasticity (STP) and long-term plasticity [43, 44]. STP is commonly manifested as paired-pulse facilitation (PPF) or paired-pulse depression (PPD), where the postsynaptic response to a second stimulus is enhanced or suppressed relative to the first [45, 46]. The PPF/PPD ratio is typically quantified as $100 \times (A_2/A_1)$, where A_1 and A_2 denote the response amplitudes of successive stimuli. Long-term plasticity typically manifests as either long-term potentiation (LTP) or long-term depression (LTD), which are induced and regulated by synaptic plasticity rules such as spike-timing-dependent plasticity (STDP) or spike-rate-dependent plasticity (SRDP) [47, 48]. Transitions from STP to LTP can be achieved by adjusting stimulation parameters such as pulse amplitude, duration, or frequency. In addition, synaptic transistors can reproduce dynamic learning-forgetting-relearning processes, a hallmark of adaptive intelligence.

Energy efficiency is a critical performance metric for synaptic transistors, particularly for large-scale neuromorphic systems. For three-terminal devices, synaptic energy consumption is commonly estimated as $E = V \times I \times t$, where V is the source-

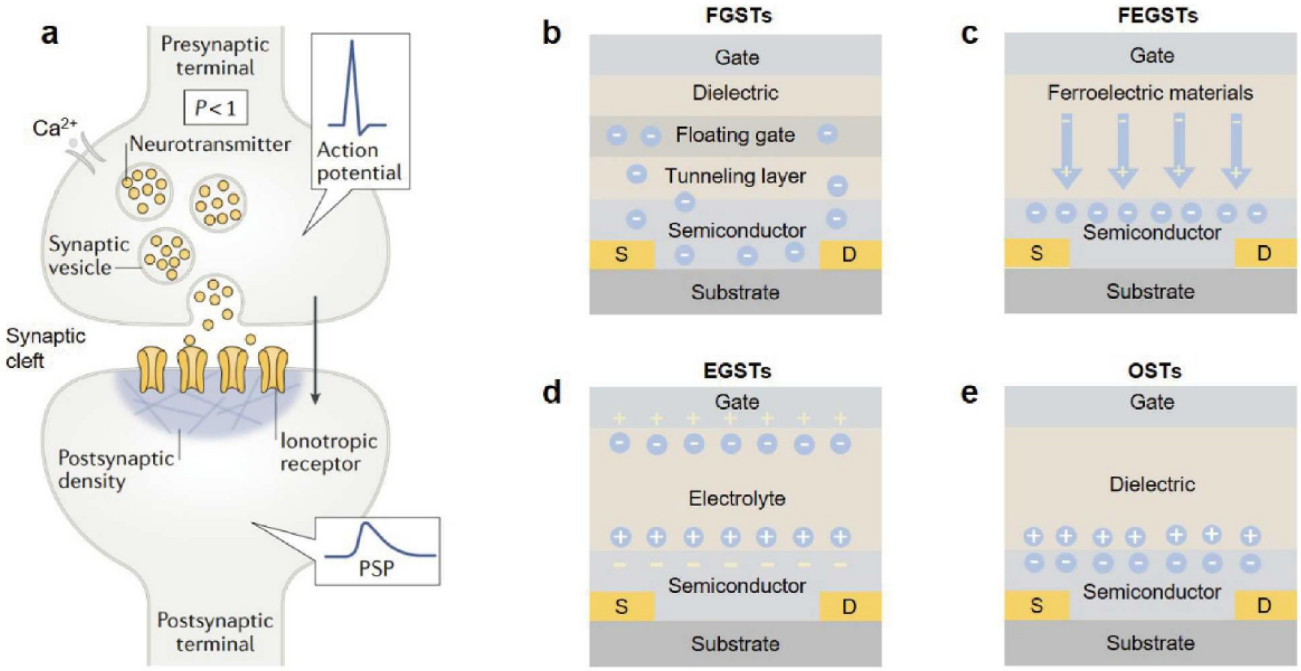

FIGURE 7 | Working mechanism of synaptic transistors. (a) The structure of a chemical synapse. Reproduced with permission [35]. Copyright 2019, Nature Reviews Neuroscience. Typical structure of (b) floating-gate, (c) ferroelectric, (d) electrolyte, and (e) optoelectronic synaptic transistors. Reproduced with permission [36]. Copyright 2025, Science China Materials.

drain voltage, I is the postsynaptic current, and t is the stimulus duration [49]. Recent advances have reduced the energy consumption of synaptic transistors to the femtojoule (1–10 fJ) level per synaptic event—comparable to, or even below, that of biological synapses. Such energy-efficient operation, combined with precise weight tunability and high endurance, positions WBG-based synaptic transistors as promising building blocks for scalable neuromorphic computing, adaptive memory systems, and low-power intelligent electronics.

3.2 | Memristors and Two-Terminal Synaptic Devices

Memristors are recognized as the fourth fundamental circuit element, complementing resistors, capacitors, and inductors, as first theoretically proposed by Chua in 1971 [32]. The defining characteristic of a memristor is that its resistance state can be continuously modulated by the history-dependent flow of electrical charge through the active medium, resulting in nonlinear and nonvolatile RS behavior. Owing to these features, memristors have been widely adopted as artificial synapses for emulating biological learning and memory functions [50]. To date, most reported memristive devices rely on electrical stimuli to regulate conductance states. Although electrically driven memristors have undergone decades of development and achieved substantial progress, optoelectronic memristors remain at a comparatively early stage. Depending on the mode of conductance modulation, optoelectronic memristors can be broadly classified into photoelectric cooperative devices, in which optical and electrical stimuli jointly regulate resistance states, and fully optical memristors, where conductance modulation is driven primarily by light. These emerging device concepts are particularly attractive for neuromorphic vision and in-sensor computing. WBGS-based memristors typically exploit defect migration, interfacial redox reactions, and either filamentary or interface-type RS [51–53]. Compared with conventional oxide memristors based on narrow-bandgap materials, WBGS memristors generally exhibit superior thermal stability, enhanced endurance, and more robust operation under high electric fields and extreme environmental conditions, making them well suited for harsh-environment neuromorphic applications.

3.2.1 | *Electronic Devices*

3.2.1.1 | *GaN.* To date, most GaN-based electrical memristors have been realized using GaN microwires (MWs) or nanowires (NWs), where low-dimensional geometries amplify defect, surface, and polarization effects. In 2016, Pan and coworkers developed a piezoelectric memristor with multilevel switching behavior based on bamboo-like GaN MWs [54]. By coupling the piezoelectric and semiconducting properties of GaN, a piezotronic modulation mechanism was introduced: Mechanical deformation induces strain-driven piezoelectric polarization at defect boundaries, which effectively modulates the internal potential landscape and reduces the SET voltage. Building on this concept, a flexible piezoelectric sensory memory device (SMD) based on bamboo-like GaN MWs was later demonstrated [55]. In this device, external strain programs the device into an HRS, whereas electrical stimuli erase it back to an LRS. The strain-induced piezopotential triggers the dissolution and redistribution of nitrogen-vacancy-based conductive channels, enabling spatially resolved mapping of tactile stimuli and memory storage. Such piezoelectric memory behavior provides a direct pathway for converting mechanical sensory information into electrical synaptic signals, highlighting the potential of GaN for interactive and multimodal neuromorphic systems. Beyond one-dimensional

GaN structures, heterostructure engineering has further expanded GaN memristor functionality. Ji et al. [56] reported a hybrid-dimensional memristor consisting of wrinkled MoS_2-wrapped GaN NWs with a spray-coated Ag NW network as the top electrode. The bipolar RS behavior is governed by the local electric fields generated by the wrinkled morphology, which drive oxygen ion migration along the NW surface to achieve memristive functionality. Separately, Huang et al. [57] fabricated bipolar GaN NW memristors via wet etching using H_3PO_4. Surface chemistry modulation alters adsorbed molecules and dangling bonds, enabling electric field-driven accumulation or depletion of oxygen vacancies and surface electrons. These studies collectively demonstrate that GaN memristors can exploit polarization effects, surface defect dynamics, and heterointerfaces to emulate complex synaptic functions. The performance comparisons in nitride-based memristors are listed in Table 2.

3.2.1.2 | *AlN.* A series of MIM-type AlN-based memristors has been demonstrated via the adoption of diverse electrode materials, including Pt, Cu, Al, Ag, Pd, and TiN. In 2013, Chen et al. [77] reported that complementary RS behavior was achieved in both TiN/AlN/Cu/AlN/TiN ECM cells and Pt/AlN/TiN/AlN/Pt ionic RS systems. Copper atoms readily undergo redox reactions in numerous semiconductors and insulators; these redox processes induce copper filament deposition, which preferentially occurs along grain boundaries or other crystalline defects of the AlN thin film. The rupture and reconnection of copper filaments trigger the HRS via thermal release and the LRS via cold release effects of the device, respectively. For the Pt/AlN/TiN/AlN/Pt device, both Pt and TiN electrodes are electrochemically inert and do not inject metal cations into the AlN film. Thus, a high-voltage electroforming process was employed to activate the ionic switching effect of the system, enabling memristive functionality. In 2016, Choi et al. [60] fabricated an Al/AlN/TiN-based memristor featuring an ultrafast switching time and relatively low switching current. They revealed that oxidation occurs at the top interface of the AlN layer, forming an AlO_xN_y phase and Al-rich conductive channels. The switching behavior of the device is dominated by the migration of nitrogen vacancies. More recently, Ling et al. [64] also developed an Al/AlN/TiN memristor with an ultrathin (~3.3 nm) AlN RS layer based on the same mechanism, achieving a retention time of 10^6 s. Furthermore, memristors based on the formation/rupture mechanism of Ag-based conductive filaments have

TABLE 2 | Performance comparisons in nitride-based memristors.

Memristors	Power consumption (pJ)	Memory window (s)	Forming voltage (V)	Retention memory window (s)	Endurance (cycles)	On/off ratio	Refs.
GaN MW	—	—	—	—	> 282	—	[54]
GaN MW	—	—	—	$> 3 \times 10^2$	> 100	~10^4	[55]
Ag/GaN MW/Ag	—	—	—	$> 10^5$	> 150	10^3	[58]
MoS_2@GaN NW	—	3.4×10^3	—	3.4×10^3	798	~10^3	[56]
H_3PO_4-treated GaN NW	—	3×10^3	0	$> 3 \times 10^3$	> 100	10^3	[57]
TiN/AlN/TiN	—	—	5, 2.5	3×10^5	10^5	> 10	[59]
TiN/AlN/Pt	—	—	—	—	—	10^2	[60]
TiN/AlN/Pt	—	—	7.8	$> 10^4$	100	—	[61]
Ag/AlN/TiN Ni/Ag/AlN/TiN	1.15	—	—	10^4	—	—	[62]
Al/AlN/TiN	—	—	4	10^4	> 120	$> 10^4$	[63]
TiN/AlN/Pt	—	—	1.51	10^6	—	> 10	[64]
Ag/AlN	—	—	—	10^4	100	> 10	[65]
Au/Al/Al_2O_3/AlN/ITO Au/Al/AlN/ITO	—	—	5	10^4	20–100	10^2–10^3	[66]
Pt/Al/TaO_x/AlN/Al_2O_3/Pt	—	—	4	$> 10^4$	100–500	> 100	[67]
Pt/HfO_x/AlN/TiN	—	—	—	$> 10^4$	500	—	[68]
Pt/Al/TiOx/HfO_2/AlN/Pt	—	—	4.16	$> 10^4$	100	—	[69]
Ag/AlN/AlScN/AlN/Pt	0.2	—	1.15	—	—	10^4	[70]
Metal/ScAlN/n-GaN	—	—	—	10^5	1000	10^5	[71]
Cu/$Sc_{0.2}Al_{0.8}N$/Pt/Ti	—	—	—	$> 10^4$	—	10^4	[72]
Au/Ti/h-BN/Au	2	1.7	—	—	> 600	> 50	[73]
Au/Ti/h-BN/Gr(E)	—	—	0	—	> 200	~10^7	[74]
Ni/h-BN/Ni	—	—	—	—	> 600	~10^7	[75]
Ag/PMMA/h-BN/Cu	—	—	—	10^5	> 800	~10^5	[76]

been extensively explored. Kwon et al. [62] developed Ag/AlN/TiN memristors, investigating their long-term and short-term memory characteristics as well as I–V curves. Additionally, they studied the switching and conduction mechanisms of Ni/Ag/AlN/TiN devices using conductive-filament schematics and energy band diagrams, opening new avenues for AlN-based memristors in neuromorphic systems (Figure 8a). Mohanty et al. [65] prepared AlN/Ag-based conductive-bridge random-access memories (CBRAMs), where the insertion of a Ta layer effectively controlled the diffusion of Ag atoms in the switching layer. Beyond single-component AlN systems, heterojunction engineering with oxides has been employed to tune memristor performance via the synergistic regulation of oxygen and nitrogen vacancies. Guo et al. [66] introduced a thin Al_2O_3 layer on the surface of the AlN film. The device performance is dominated by the nitrogen-vacancy conductive-filament mechanism, and the Al_2O_3 layer stabilizes the conductive path by providing additional oxygen vacancies, thereby enhancing device performance in memory and computing applications. Recently, Choi et al. [67] embedded a 1.2-nm-thick AlN layer between the TaO_x switching layer and the Al_2O_3 tunnel barrier layer, which acts as a built-in current limiter. This design facilitates controlled filament formation and achieves intrinsic adaptability without the need for external circuits. The resulting $Pt/Al/TaO_x/AlN/Al_2O_3/Pt$ RRAM device enables polarity-dependent dual-mode switching within a single cell. Similarly, the $Pt/Al/TiO_x/HfO_2/AlN/Pt$ device fabricated by Park et al. [69] exhibits abrupt filamentary RS behavior, whose characteristics are strongly dependent on the variation of defect states in the TiO_x layer. A natural oxidation reaction between the TiO_x oxygen reservoir and the Pt/Al top electrode forms an AlO_x layer serving as an overshoot suppression layer (OSL). Moreover, an ultrathin AlN layer at the interface between the HfO_2 layer and the Pt/Ti bottom electrode acts as an oxygen barrier layer (OBL), effectively inhibiting oxygen ion migration.

3.2.1.3 | *BN.* Within BN, amorphous BN (*a*-BN) and h-BN have been extensively employed for memristors. Similar to other nitride-based memristors, the MIM architecture is predominantly adopted for BN-based devices, where the formation/rupture of CFs remains the dominant physical mechanism underlying nonvolatile RS. Currently, MIM-structured BN memristors typically consist of an active metal top electrode (e.g., Ag, Cu), a BN functional layer, and an inert metal bottom electrode (e.g., Pt, Au), featuring high spatial utilization and integration density. *a*-BN exhibits a disordered atomic arrangement without long-range order. Its ultrawide bandgap (> 6 eV) and low dielectric constant ($\kappa \approx 1.8$) render it an ideal candidate for conventional memristor architectures [79]. Khot et al. [18] demonstrated a CMOS-compatible Ag/*a*-BN/Pt memristor tailored for neuromorphic applications. By modulating the current compliance (I_{cc}) of the *a*-BN functional layer, multilevel RS was achieved, enabling multibit storage capability with 10^4 endurance cycles and a nonvolatile retention time exceeding 10^6 s while maintaining distinct resistance-state discrimination. In contrast, h-BN comprises vertically stacked 2D planes interconnected via van der Waals (vdW) forces. Its atomic-scale thickness and exceptional insulating properties make it an ideal platform for investigating interfacial charge dynamics and quantum mechanical tunneling effects

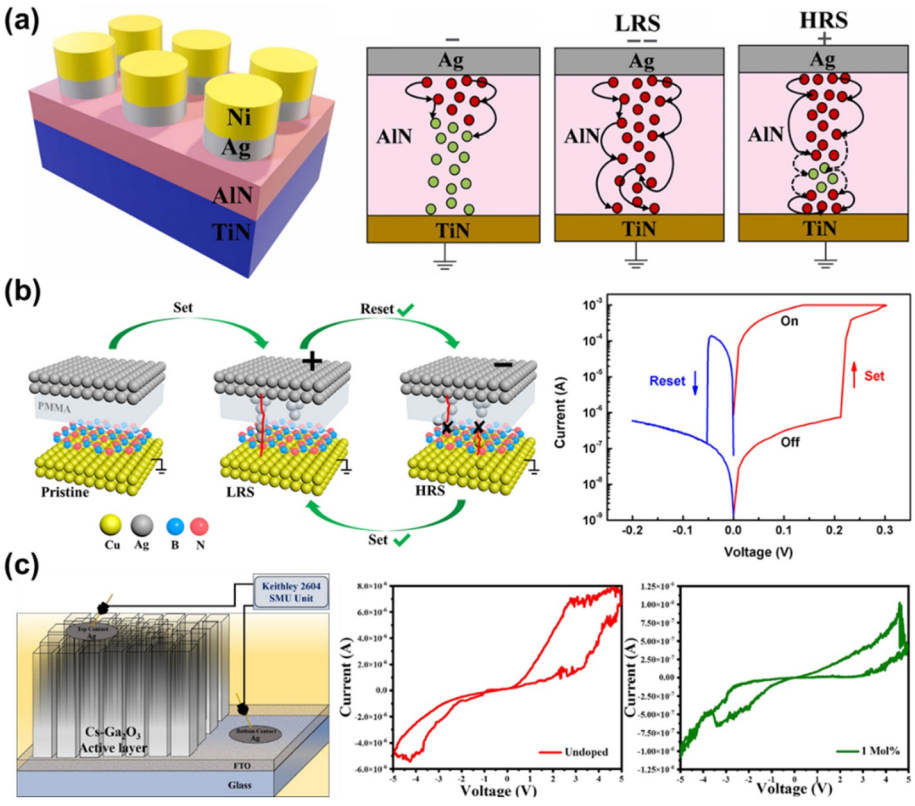

FIGURE 8 | Memristors and their working mechanisms. (a) Ag/AlN/TiN. Reproduced with permission [62]. Copyright 2022, Journal of Alloys and Compounds. (b) Ag/PMMA/h-BN/Cu. Reproduced with permission [76]. Copyright 2021, Materials & Design. (c) Cesium-doped Ga_2O_3 ($Cs\text{-}Ga_2O_3$). Reproduced with permission [78]. Copyright 2022, Memories – Materials, Devices, Circuits and Systems.

in nanoscale memristive systems. Intrinsic lattice defects (e.g., vacancy clusters, grain boundaries) in CVD-synthesized h-BN serve as preferential pathways for metal ion migration from electrodes, facilitating controllable CF formation via ECM. Völkel et al. [75] developed a bilayer Ni/h-BN/Ni crossbar memory, achieving an on/off ratio exceeding 10^7 at operating voltages below 3 V. Teja Nibhanupudi et al. [73] designed an Au/Ti/h-BN/Au memristor with a multilayer 2D structure, leveraging the intrinsic defect tolerance of CVD-grown h-BN to realize ultrafast switching speeds below 5 ns. To optimize device performance, heterostructure engineering and interface modulation have been widely explored. Ge et al. [76] fabricated an Ag/PMMA/h-BN/Cu structured device by inserting a PMMA interfacial polymer layer between the monolayer h-BN and the top electrode (Figure 8b). This design effectively restricts CF dimensions and suppresses excessive CF formation on the bottom Cu electrode, endowing the device with low operating voltage, high on/off ratio, and long retention time. When combined with carbon-based materials, carbon ions form conductive carbon filaments, thereby achieving memristive properties. Xie et al. [74] developed vertical h-BN memristors with graphene edge contacts. Then, several graphene/h-BN heterostructured memristors, i.e., G/h-BN/G/SiO_2/Si [80], Ti/MLG/h-BN/MLG/Au [81], and Au/Ti/G/h-BN/G/Au [82], were proposed. Suzuki et al. [83] successfully grew h-BN layers on both single carbon nanotubes and carbon nanotube bundles via dry-spinning technology and fabricated h-BN/CNT heterostructure memristor devices. The device's resistive behavior originates from the disordered amorphous carbon structure between h-BN layers, wherein carbon atoms penetrate the hexagonal BN layers to form conductive pathways, inducing a transition from an HRS to an LRS.

3.2.1.4 | *SiC.* Within the SiC family, amorphous SiC (*a*-SiC), β-SiC, and 4H-SiC have been exploited for memristor fabrication. SiC-based memristors typically rely on electrical pulse-induced metal ion migration to trigger the formation and rupture of metallic CFs within the SiC active layer. This process efficiently modulates device conductivity, endowing the devices with memristive characteristics. In 2011, Lee et al. [84] first reported an *a*-SiC-based RRAM. Employing sputtered SiC as the insulating layer and Cu as the active electrode, the device achieved 10^5 endurance cycles and a two-order-of-magnitude on/off ratio by incorporating a germanium antimony telluride (GeSbTe) barrier layer. Zhong et al. [85] demonstrated a Cu/*a*-SiC/Au memristor with an ultrahigh on/off ratio of 10^9. Chen et al. [86] introduced a titanium antimony telluride (TiSbTe) layer into *a*-$SiC_{0.11}$:H memristors, which enhanced the switching uniformity of the devices. This improvement was attributed to the formation of Si dangling bond nanochannels within the TiSbTe layer. For single-crystalline SiC devices, Liu et al. [87] simultaneously achieved threshold switching (TS) and bipolar RS behaviors in a single Ag/4H-SiC/Pt device by tuning the I_{cc}. Qin et al. [88] proposed a full electron-beam evaporation approach to fabricate Cu/SiC/Pt structures on 2-inch intrinsic Si substrates, realizing the transition from volatile to nonvolatile switching. The device exhibited low symmetric switching voltages of ± 0.5 V, > 200 cycling endurance, > 10^3 s retention time, an on/off ratio of ~10^3, and at least six stable resistance states. Kapur et al. [89] developed a memristor based on back-end-of-line (BEOL)-compatible SiC, demonstrating excellent bipolar switching behavior with an on/off ratio of 10^4. A 3 × 3 artificial synaptic array constructed from these devices successfully emulated synaptic functions corresponding to the "learning-forgetting-relearning" process. Recently, the same group fabricated SiC/Si bilayer resistive memory via plasma-enhanced chemical vapor deposition (PECVD) [90]. Precise modulation of resistance states and multilevel switching were achieved by varying pulse conditions, with the device exhibiting over 10^9 endurance cycles at an on/off ratio of ~10^2. Santra et al. [91] reported a bipolar RS device with low power consumption and high performance based on a ZnO@β-SiC composite, which eliminated the need for a preforming process. Embedded Zn_2SiO_4 nanocrystals within the amorphous matrix enabled device stabilization up to 10^4 cycling endurance and 10^4 s retention time, governed by the CF formation and dissolution mechanisms driven by oxygen vacancies and metal cations. The performance comparisons in SiC-based memristors are listed in Table 3.

3.2.1.5 | *Ga_2O_3.* The core RS mechanisms of Ga_2O_3-based memristors are centered on oxygen-vacancy (*Vo*) migration, predominantly falling into two categories. The first is the CF mechanism, where nanoscale conductive channels are formed by the aggregation of *Vo* or metal cations (e.g., Ag^+), with the transition between HRS and LRS achieved through CF formation (SET process) and rupture (RESET process), featuring fast switching speeds and high on/off ratios. The second is the ionic-electronic conduction mechanism, in which oxygen ion migration across a broad region modulates the bulk conductivity of the film, enabling gradual switching characteristics that are well suited for neuromorphic synaptic applications. In terms of fabrication and device architecture, Ga_2O_3 memristors are mainly fabricated via RF sputtering, pulsed laser deposition (PLD), and electron-beam evaporation. The mainstream device configuration is the vertical MIM structure, with electrode materials including inert metals (Pt, Au), active metals (Ag, Cu, Al), and transparent conductive oxides (ITO). Device performance can be optimized by incorporating buffer layers such as graphene oxide (GO) and WO_3, as summarized in Table 4. Regarding performance trends, amorphous Ga_2O_3 thin films exhibit low leakage current and superior on/off ratios (up to 10^8), whereas β-Ga_2O_3 annealed at 600°C–800°C demonstrates enhanced stability [97]. Recently, He et al. [98] successfully constructed vertical Ag/β-Ga_2O_3/Pt memristors on high-crystalline-quality β-Ga_2O_3 films via lattice epitaxy engineering and sacrificial-layer-assisted transfer, achieving an on/off ratio exceeding 10^8. Using a scalable polymer-assisted deposition method, Dai et al. [99] prepared ferromagnetic amorphous gallium manganese oxide (*a*-GMO) films with a tunable Mn-dopant two-level system. The resulting Pt/*a*-GMO/Pt memristors delivered an on/off ratio of up to 10^3, benefiting from the synergistic effect of Vo-induced LRS and Mn^{2+}-enhanced HRS. Suman et al. [78] deposited cesium-doped Ga_2O_3 (Cs-Ga_2O_3) nanostructured films via a one-step wet chemical method (Figure 8c). The presence of metal ions near the bottom electrode facilitates rapid CF formation, whereas Cs doping enables spontaneous diffusion of vacancies in the insulating layer, reducing the *Vo* concentration below a critical threshold to induce CF rupture, thus yielding a retention memory window of 10^5 s. Despite

TABLE 3 | Performance comparisons in SiC-based memristors.

Memristors	Power consumption (pJ)	Memory window (s)	Forming voltage (V)	Retention memory window (s)	Endurance (cycles)	On/off ratio	Refs.
TiN/GST/Cu/SiC/Pt	10^5–10^6	—	—	$> 10^4$	$> 10^4$	$> 10^3$	[84]
Cu/α-SiC/Au	—	—	—	—	—	10^9	[85]
Ag/4H-SiC/Pt	3.225×10^{-2}	—	—	$> 10^5$	—	—	[87]
Cu/SiC/W	—	—	5	10^3	100	$> 10^3$	[89]
SiC/Si	—	—	8.5	—	10^9	10^2	[90]
Ag/ZnO@β-SiC/Pt	10^5	10^3	0	10^4	10^4	25	[91]
ITO/ZnO@β-SiC/Ag	—	—	—	10^4	10^4	10^3	[92]
Cu/SiC/Pt	—	—	—	—	150	10^3	[93]
Ti/Cu/SiC/Pt	—	—	—	$> 10^3$	> 200	~10^3	[88]
Al/TiSbTe/α-$SiC_{0.11}$:H/Si^+	—	10^2	0	10^4	10^3	—	[86]
Al/Ag NPs:α-$SiC_{0.11}$:H/Al	—	—	—	10^4	10^4	10^7	[94]

TABLE 4 | Performance comparisons in Ga_2O_3-based memristors.

Memristors	Power consumption (pJ)	Memory window (s)	Forming voltage (V)	Retention memory window (s)	Endurance (cycles)	On/off ratio	Refs.
Ag/Ga_2O_3/Au	—	10^3	2.4	10^4	$> 1.1 \times 10^4$	$> 10^3$	[95]
Al/Ga_2O_3/Pt/Ti	—	—	4	—	4×10^3	$> 10^5$	[96]
Ag/Ga_2O_3/Pt	—	—	4.9	10^6	—	—	[97]
Ag/β-Ga_2O_3/Pt	—	—	0.5	4×10^4	125	$> 10^8$	[98]
Pt/α-GMO/Pt	10^5–10^6	10^3	—	10^3	150	10^3	[99]
Au/Ti/β-Ga_2O_3/Ti/Au	—	10^2	—	10^3	200	10	[100]
Pt/α-GaO_x/ITO	—	—	—	—	—	10^2	[101]
Al/α-Ga_2O_3/ITO	—	10^2	−8	10^4	100	10^3	[102]
Ag/Cs-Ga_2O_3/FTO	—	10^2	—	10^5	—	10	[78]
Al/GO/α-Ga_2O_3/ITO	—	10^2	—	1×10^2	100	10^3	[103]
Cu/TiW/Ga_2O_3/Pt	—	> 10	—	$> 10^5$	> 140	10^2	[104]
Ga/GaO_x/SiO_x/p-Si	—	—	—	10^8	10^5	10^2	[105]
Pt/Ga_2O_{3-x}/SiC/Pt	—	10^2	—	1×10^2	—	10^3	[31]
Ga_2O_3/ZnO composite films	—	—	—	10^4	100	4.0×10^2	[106]
Cu/TiW/IGZO/Ga_2O_3/Pt	—	10^4	5.1	10^4	$> 10^3$	$> 10^3$	[107]

these advancements, Ga_2O_3 memristors generally exhibit cycling endurance of 10^2–10^3 cycles and data retention of 10^3–10^4 s, along with capabilities for multilevel and analog switching. However, their endurance remains inferior to that of mature oxide-based materials, necessitating further structural optimization for performance enhancement. The performance comparisons in Ga_2O_3-based memristors are listed in Table 4.

3.2.1.6 | *Diamond.* Diamond-based memristors exploit unique sp^2–sp^3 carbon phase transitions and defect dynamics. As listed in Table 5, Battistoni et al. [108] reported Ti-doped

diamond memristors in which RS arises from dehydrogenation/hydrogenation-induced sp^2–sp^3 transitions, enabling reproducible short- and long-term synaptic plasticity. Liu et al. [109] developed an ultralow-threshold-voltage-responsive synaptonic memristor based on a Cu_xO and bromine-doped diamond (BDD) heterojunction. The HRS and LRS corresponding to oxygen-vacancy clusters form the basis of its hysteretic behavior. Synaptic functionality remains observable even when pulse amplitude is reduced to an ultralow value of 3 mV, with energy consumption as low as 9.5×10^{-11} J.

3.2.2 | *Optoelectronic Devices*

The broken inversion symmetry of wurtzite GaN gives rise to pronounced spontaneous and piezoelectric polarization along the *c*-axis, which critically governs its optical and electrical responses. In optoelectronic synaptic devices, polarization-induced built-in electric fields generate potential wells that regulate carrier trapping, separation, and release, thereby enabling history-dependent conductance modulation. Integrating GaN with other strongly polar or wide-bandgap materials has thus emerged as an effective strategy to realize polarization-modulated optoelectronic memristive behavior.

Hua et al. [110] demonstrated a ultraviolet (UV) optical synaptic device based on a GaN/AlN periodic heterostructure, exhibiting persistent photocurrent (PPC) originating from strong polarization fields at GaN/AlN interfaces. Xie et al. [111] fabricated a dual-port nonvolatile reconfigurable electro-optic dual-mode memristor based on an n-GaN/i-GaN/AlScN heterojunction, where the i-GaN and AlScN layers govern the photoresponsive and storage properties, respectively. The device achieves an on/off ratio of ~10^4 in both electrical and optoelectronic modes, with reliable resistance-state resetting, writing, and long-term retention. Nanostructured GaN platforms further enhance optoelectronic plasticity by amplifying polarization and surface-state effects. As shown in Figure 9a, Ji et al. [112] prepared amorphous-oxide-modified GaN NW arrays (GaO_x@GaN NWAs) on flexible graphite paper, exhibiting an ultralong decay time of 2.3×10^6 s. Similarly, Liu et al. [114] proposed a photoelectrochemical synaptic device based on p-AlGaN/n-GaN NWs. Internal p-n junctions formed during NW growth on n-Si substrates modulate carrier behavior, and two opposing built-in electric fields enable hole storage in NWs, leading to history-dependent synaptic behaviors. Beyond binary synaptic emulation, advanced bandgap and polarization engineering enable functional diversification. Gao et al. [115] reported a multifunctional optoelectronic synapse with an n-GaN/i-GaN/AlN multiple-quantum-disk (MQD)/n-GaN architecture. Under 254 nm illumination, efficient carrier confinement by AlN barriers and restricted carrier separation within the n-i-n structure allow the device to emulate both parvocellular and

TABLE 5 | Performance comparisons in diamond-based memristors.

Memristors	Power consumption (pJ)	Memory window (s)	Forming voltage (V)	Retention memory window (s)	Endurance (cycles)	On/off ratio	Refs.
Titanium-doped diamond	—	—	—	$> 10^5$	> 150	10^2–10^3	[108]
Cu_xO and B-doped diamond (BDD) heterojunctions	95	—	—	—	—	—	[109]

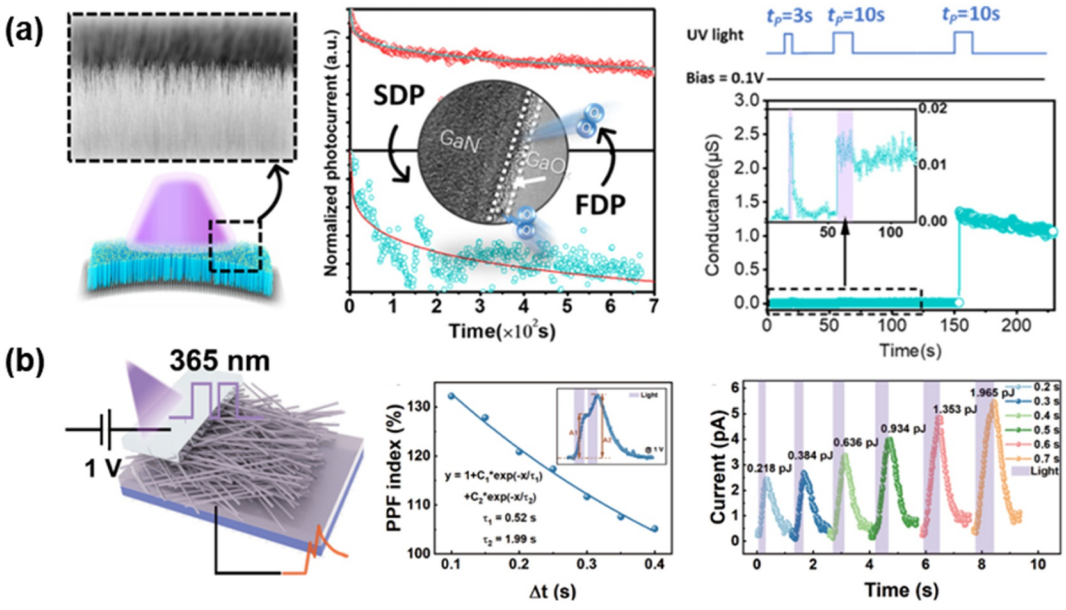

FIGURE 9 | Optoelectronic memristors based on (a) GaO_x@GaN NWAs on flexible graphite paper, reproduced with permission [112]. Copyright 2022, Applied Materials; and (b) SiC/SiO_2@Ag NW network device. Reproduced with permission [113]. Copyright 2025, Science China Materials.

magnocellular pathways in the human retina, enabling contrast-sensitive and motion-sensitive visual processing within a single hardware platform.

Optoelectronic memristive behavior has also been demonstrated in other WBG systems. Chen et al. [113] realized a SiC/SiO_2@Ag NW network device capable of UV-responsive synaptic behavior under zero-bias illumination and electrically driven synaptic modulation under external bias (Figure 9b). Benefiting from local field enhancement and localized surface plasmon resonance (LSPR) in Ag nanoparticles, the device operates at ultralow energy consumption (~0.471 fJ per synaptic event). Zhang et al. [116] fabricated a monolithic 4 × 4 array of vertical Schottky barrier diodes on heavily doped 4H-SiC substrates, where defect-assisted carrier dynamics enable programmable synaptic responses under visible-light excitation. Feng et al. [117] prepared a GaN/Ga_2O_3/GaN back-to-back double heterojunction device, integrating fast photoresponse and PPC effect by regulating the ionization and deionization of V_o in Ga_2O_3. Finally, Mizuno et al. [118] first demonstrated a photomemristor based on vertically aligned graphene (VG)/diamond heterojunctions. Owing to redox reactions occurring at the graphene layer and/or graphene/diamond (sp^2/sp^3 carbon) interface, the device achieved light-controlled EPSC, STM-LTM conversion, and PPF with a photovoltaic coupling index exceeding 300%. The device array further functions as an image-sensing memory capable of selective optical information storage. The performance comparisons in WBGS-based memristors and two-terminal synaptic devices are listed in Tables 6 and 7.

3.2.3 | *Ferroelectric Devices*

Ferroelectric materials are intrinsically well suited for neuromorphic computing due to their nonvolatile polarization states, low switching energy, and ultrafast response times. By electrically reversing spontaneous polarization, ferroelectric layers can modulate carrier accumulation, depletion, and transport barriers in adjacent semiconductor channels, thereby enabling analog, nonvolatile SW storage. In typical metal-ferroelectric-metal (MFM) junctions, polarization charges at ferroelectric/metal interfaces are partially screened by free carriers in the electrodes. Asymmetric screening lengths at the two interfaces result in unequal electrostatic potentials, giving rise to polarization-dependent energy barriers. Assuming different Thomas–Fermi screening lengths ($\delta_1 > \delta_2$) for electrodes M_1 and M_2, the electrostatic potential φ varies asymmetrically across the junction (Figure 10a), and polarization reversal directly reshapes the transport landscape, switching the device between high- and low-resistance states. Depending on ferroelectric thickness and barrier profile, charge transport may proceed via direct tunneling, Fowler–Nordheim tunneling, or thermionic emission (Figure 10b–d). The performance comparisons in WBGS-based ferroelectric memristors are listed in Table 8.

In recent years, memristors based on AlN/ScAlN systems and 2D vdW ferroelectric materials have emerged as research hotspots in storage and neuromorphic computing, with numerous high-performance devices successfully developed and their application potential validated. 2D vdW ferroelectric materials attract significant attention due to their electrical tunability, low-power switching, and strong light–matter interactions. Their layered structure facilitates the fabrication of stable monolayer/few-layer samples, offering an ideal platform to investigate lattice dimensionality effects on long-range ferroelectric order. Integrating these materials into GaN high-electron-mobility transistors (HEMTs) enables low subthreshold swing and advanced neuromorphic computing.

In 2022, Liu et al. [147] designed an AlScN ferroelectric diode-based memristor, realizing 4-bit pulse-programmable storage and laying the foundation for novel ferroelectric materials in compute-in-memory (CIM) platforms. Concurrently, Wang's group [144] developed a fully epitaxial ScAlN/GaN heterojunction device, exhibiting a high rectification ratio, long retention, and excellent endurance thanks to its ultrawide bandgap and high Curie temperature. Its RS relies on ferroelectric polarization-modulated interfacial carrier concentration: Positive pulses induce downward polarization (charge accumulation, ON state), whereas negative pulses trigger upward polarization (electron depletion, OFF state). To address the insufficient on/off ratio and high operating voltage in early devices, Mi's group [71] tuned the ScAlN thickness to 9 nm, leveraging the synergy between its native oxide layer and ferroelectric polarization to achieve a 10^4–10^5 on/off ratio and low read/write voltages (< 3 V/8 V).

Beyond single-layer ferroelectrics, structural and material innovations have further expanded device capabilities. Han et al. [72] proposed a Cu/$Sc_{0.2}Al_{0.8}N$/Pt/Ti MIM memristor with defect-assisted conduction. It demonstrated an on/off ratio > 10^6, retention > 10,000 s, and cycling stability > 200 cycles, enabling multilevel switching, emulating synaptic behaviors (LTP, PPF), and completing MNIST handwritten digit recognition (Figure 11). Choi et al. [67] designed a Pt/Al/TaO_x/AlN/Al_2O_3/Pt device, achieving polarity-dependent dual-mode switching via a 1.2-nm AlN built-in current limiter—abrupt digital switching (forward bias) and gradual analog modulation (negative bias)—with 93.5% classification accuracy on the modified MNIST dataset. To overcome electrical-only control limitations, Xie et al. [6] developed an electro-optic dual-mode memristor based on an n-GaN/i-GaN/AlScN heterojunction, synergizing AlScN's ferroelectric storage and GaN's optoelectronic response to switch resistance states via light-modulated polarization reversal thresholds.

Finally, the integration of 2D vdW ferroelectrics further enriches WBG neuromorphic platforms. Yang et al. [148] integrated α-In_2Se_3 (room-temperature reversible out-of-plane/in-plane polarization) into GaN-based MOS-HEMTs. A self-aligned structure enhanced out-of-plane polarization and suppressed in-plane polarization, achieving a 10-mV/dec subthreshold swing and emulating synaptic behaviors (STP, PPF). Park et al. [146] heterogeneously integrated $CuInP_2S_6$ (CIPS) ferroelectric films as gate dielectrics with AlGaN/GaN HEMTs, realizing SW programming via polarization-induced switching and simulating artificial neural networks (ANNs) through LTP/LTD emulation. These studies advance ferroelectric-based memristors toward high performance, multifunctionality, and low power consumption via material composition regulation, structural innovation, and mechanism exploration, providing crucial support for high-density storage and energy-efficient neuromorphic computing.

TABLE 6 | Performance comparisons in WBGS-based optoelectronic memristors.

Memristors	Wavelength optical power	Power consumption (pJ)	Memory window (s)	Forming voltage (V)	Retention memory window (s)	Endurance (cycles)	On/off ratio	Synaptic/ neuronal functions	Refs.
n-GaN/i-GaN/AlScN	355 nm	—	—	—	—	—	10^4	—	[111]
p-AlGaN/n-GaN NW	255 nm 12 μW/cm^2	—	60	—	1.5×10^4	—	—	—	[114]
n-GaN/i-GaN/AlN MQDs/ n-GaN	254 nm 0.553 mW/cm^2	—	0.85	—	32.57	—	—	—	[115]
GaO_x@GaN	365 nm 8.4 mW/cm^2	—	—	—	2.3×10^5	—	~10^3	—	[112]
InSe/GaN	300–780 nm 40 mW/cm^2	—	—	—	—	—	10^3	—	[119]
SiC/SiO_2@Ag NWN	365 nm 46–246 mW/cm^2	0.471×10^{-3}	0.4	—	0.9	—	—	—	[113]
Ag/SiC/SiO_2@Ag (NWN)/ITO	365 nm 326 mW/cm^2	5.936×10^{-3}	—	—	0.9	—	—	—	[113]
Cu/TiW/Ga_2O_3/Pt	254 nm 130 μW/cm^2	—	$> 10^5$	—	—	> 140	—	—	[120]
Pt/Ga_2O_3/Pt	365 nm 0.067–0.471 mW/cm^2	—	10^4	5	—	10^4	$> 10^4$	—	[121]
Ag/Zn-doped Ga_2O_3 (ZGO)/Ag	254 nm 15.70 μW/cm^2	28×10^{-3}	—	—	—	—	—	—	[122]
ITO/*a*-Ga_2O_3/Pt	254 nm 10 μW/cm^2	—	—	—	> 3600	10^6	10^3	—	[123]
Ti-Ga_2O_3 NW-Au	255 nm 0.16 mW/cm^2	23.9	—	—	—	—	—	—	[124]
Ag/β-Ga_2O_3 microwire/Ag	254 nm 1000 μW/cm^2	—	—	—	—	—	10^3	—	[125]
M1/CNW-diamond/M2	—	—	—	—	1.374×10^4	—	—	—	[29]
NUNCD-Si/NUNCD-SCD	400–900 nm 1.1–4.3 mW/mm^2	—	—	—	—	> 800	—	—	[126]
Ni/vertical graphene (VG)/ B-doped diamond	470 nm 78 μW/cm^2	0.44	5.4	—	1.558×10^3	—	10^2	—	[118]

(Continues)

TABLE 6 | (Continued)

Memristors	Wavelength optical power	Power consumption (pJ)	Memory window (s)	Forming voltage (V)	Retention memory window (s)	Endurance (cycles)	On/off ratio	Synaptic/neuronal functions	Refs.
Ag/ITZO/Ga_2O_3/ITO	275–550 nm 40–225 μW/cm^2	—	—	—	—	—	—	LTD/LTP PPF/PPD STP/LTP	[127]
Ag/Ga_2O_3/MoS_2/ITO	365 nm 0.110–3.290 mW/cm^2	—	—	—	> 500	$> 8 \times 10^3$	—	PPF/PPD STP/LTP STM/LTM	[128]
Ag/Ga_2O_3/Pt	254 nm 0.8–2.4 mW/cm^2	61.36 544.89	—	3	$> 1 \times 10^4$	80	6.1×10^5	PPF SIDP SNDP STDP SFDP STM/LTM	[129]

Abbreviations: EPSC/EPSP, excitatory postsynaptic currents/potentials; IPSC/IPSP, inhibitory postsynaptic currents/potentials; LTD, long-term depression; LTM, long-term memory; LTP, long-term potentiation; PPC, persistent photocurrent; PPD, paired-pulse depression; PPF, paired-pulse facilitation; QCSE, quantum-confined Stark effect; SFDP, spike-frequency-dependent plasticity; SIDP, spike-intensity-dependent plasticity; SNDP, spike-number-dependent plasticity; SRDP, spike-rate-dependent plasticity; STDP, spike-timing-dependent plasticity; STM, short-term memory; STP, short-term plasticity.

3.3 | Synaptic Transistors

Synaptic transistors represent a key class of neuromorphic devices that enable gate-tunable and highly controllable synaptic plasticity. Unlike two-terminal memristors, three-terminal transistor architectures decouple signal transmission and weight modulation, allowing simultaneous read and learning operations with minimal cross talk. Synaptic transistors based on GaN HEMTs, SiC metal-oxide-semiconductor field-effect transistors (MOSFETs), and related WBG platforms have attracted increasing attention owing to their high carrier mobility, robust thermal stability, and compatibility with advanced semiconductor processing. In these devices, polarization fields, charge trapping/detrapping at dielectric interfaces, and gate-controlled electrostatic modulation play decisive roles in enabling analog and nonvolatile weight tuning. The concept of employing transistors for neuromorphic computing dates back to 1996, when Mead et al. [149] first demonstrated transistor-based artificial synapses. Since then, synaptic transistors have shown clear advantages in emulating biological synaptic functions, including high-precision and continuous modulation of SW, flexible structural design, and intrinsic compatibility with large-scale integration. Moreover, multigate and dual-gate synaptic transistors exhibit structural and functional similarities to biological dendrites, providing a promising route toward advanced synaptic behaviors such as nonlinear integration, spatial summation, and context-dependent learning.

3.3.1 | *Electronic Transistors*

Electronic synaptic transistors based on WBGSs primarily exploit gate-controlled charge trapping, defect-mediated relaxation, and ionic motion to emulate synaptic plasticity. Their three-terminal configuration enables precise and decoupled modulation of channel conductance, providing advantages in controllability and endurance over two-terminal counterparts. As listed in Table 9, Li et al. [150] proposed an innovative neuromorphic engineering strategy, utilizing unique dendritic dislocations within GaN HEMTs that extend from the bulk material to the channel. Gate voltage (V_G) activates these defect states to trap carriers, whereas gradual detrapping after bias removal produces a characteristic PSC decay, closely mimicking biological synaptic relaxation. Kim et al. [152] fabricated fluorine-doped β-Ga_2O_3 thin-film transistors (TFTs) with an ultrathin channel thickness of ~10 nm by controlled reactive ion etching. Electron trapping at the gate dielectric and F-β-Ga_2O_3/SiO_2 interface dominates synaptic behavior, enabling a high on/off ratio (1.61×10^5), low subthreshold swing (90 mV·dec^{-1}), and stable analog modulation.

Ionically coupled synaptic transistors further enrich the functionality of electronic devices. Lin et al. [153] developed a sodium-doped Ga_2O_3 three-terminal electrolyte-gated synaptic transistor (EGST), where sodium ion migration modulates channel conductivity under different gate voltages, emulating the signal transmission mechanism in biological synapses. The EPSC under low positive gate voltage resembles short-term memory (STM), whereas the EPSC under high positive gate voltage simulates long-term memory (LTM). Li et al. [154] fabricated vertical short-channel Ga_2O_3 TFTs, featuring an ultrashort channel length of ~10 nm due to the vertical structure design. This device not only operates stably at a low voltage

TABLE 7 | Performance comparisons in WBGS-based two-terminal synaptic devices.

Type	Materials	Device size	Stimulus signal	Spike width (s)	Per-spike energy consumption (pJ)	Synaptic/ neuronal functions	Refs.
Planar	AlN/sapphire templates	505 × 560 μm	Pulse Xe flash lamp, 50–200 Hz V_{DS} = 30 V	5×10^{-10}	—	EPSC IPSC PPF STP/LTP LTD	[130]
Vertical	p-i-n GaN/AlN	—	UV 365 nm −40 V	0.2	—	EPSC PPF STM/LTM STDP	[110]
—	Ti/GaN NWs/Au	—	UV 365 nm 5 V	1	2.72	EPSC PPF STM/LTM	[131]
—	p-AlGaN/n-GaN NWs	—	255 nm	0.2	—	STP/LTP PPF	[114]
—	p-GaN/n-AlGaN/ n-GaN NWs		265 nm	2.5	Self-powered	STP/LTP PPF	[132]
Vertical	AlGaN/GaN/Au	—	340 nm 2 V	1	—	EPSC PPC	[133]
Vertical	n-GaN/MQDs/ n-GaN	—	254 nm 1 V	1	—	PPC PPF SNDP SRDP QCSE STM to LTM	[115]
Vertical	Ti/Al/Ti/4H-SiC/ Ti/Al/Ti	—	405 nm 2 V	0.3	5.6×10^4	EPSC PPF STP/LTP	[116]
—	Ag/Ga_2O_3/ ZnO/ITO	—	DUV 254 nm 1 V	2	6.64×10^7	EPSC PPF STP/LTP	[134]
—	Ti/Au/β-Ga_2O_3	3 × 3 rray	DUV 10 nW/cm^2	0.5	5×10^3	STP	[135]
—	Au/a-Ga_2O_3/Si/In	—	254 nm 1 V	2	2.36×10^6	PPF PPC STM/LTM	[136]
—	ITO/a-Ga_2O_3/ ZnO/ITO	W, L = 2 mm	DUV 265 nm 0.6 V	0.05	0.316	EPSC PPF STP/LTP	[137]
—	GTO/Al/HfO_x	W = 1000 μm L = 30 μm	DUV 254 nm 0.5 V	0.5	390	EPSC PPF LTD/LTP SRDP	[138]
—	Ti/β-Ga_2O_3/Au	W = 5 μm L = 5 μm	DUV 258 nm	0.2	2.5×10^{-2}	STP LTP/LTD	[139]
Vertical	Ni/VG/diamond	/	470 nm 8 V	0.05	440	EPSC PPF STM/LTM	[118]
—	Ti/GaN/Ga_2O_3/ GaN/Au	—	254 nm 5 V	1	584	EPSC PPF STP/LTP	[117]

(Continues)

TABLE 7 | (Continued)

Type	Materials	Device size	Stimulus signal	Spike width (s)	Per-spike energy consumption (pJ)	Synaptic/ neuronal functions	Refs.
—	p-n 4H-SiC	$W = 25\ \mu m$ $L = 500\ \mu m$	375 nm 5 mV	20 ms	0.23	EPSC PPF STDP SRDP SNDP	[140]
—	$Pt/Ga_2O_3/Pt$	—	365–660 nm 0.5 V	0.5 s	—	PPF STM/LTM	[141]

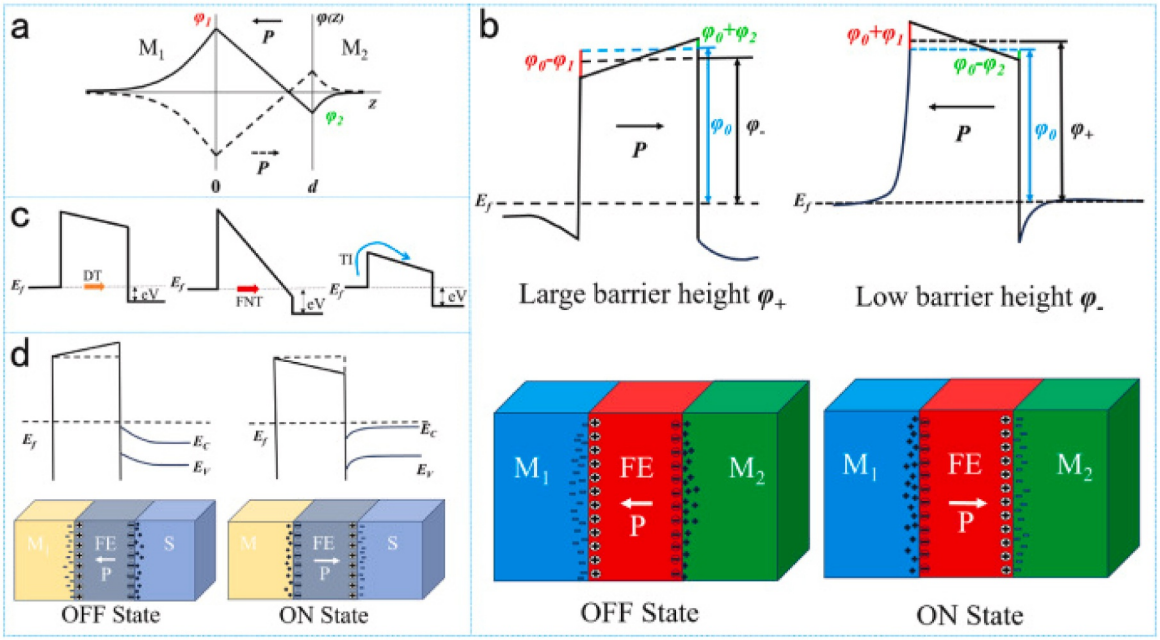

FIGURE 10 | Schematic of ferroelectric polarization-controlled resistive switches. (a) Corresponding asymmetric electrostatic potential distribution (solid line). Dashed lines indicate the potential when polarization P switches in the ferroelectric device (assuming shielding length L_1 of M is greater than L_2). (b) Large low-ferroelectric tunnel barriers along different polarization directions in the MFM structure, yielding "off" and "on" states, respectively. (c) Three possible transport mechanisms demonstrated via ultrathin ferroelectric layers: direct tunneling (DT), Fowler–Nordheim tunneling (FNT), and thermionic emission (TI). (d) Construction of a ferroelectric tunnel junction using the metal-ferroelectric-semiconductor (MFS) structure and corresponding band diagrams. Reproduced with permission [142]. Copyright 2025, Materials Today Physics.

(2 V) with a reasonable on/off ratio of 10^3 but also enables spatiotemporal logic encryption by regulating ion coupling paths. Additionally, heterostructured vdW systems have been explored for programmable synaptic behavior. Li's group [151] reported a heterogenized programmable p-n junction based on WSe_2/h-BN/Gr, where part of the WSe_2 channel lies above graphene with a separation of ~20 layers of h-BN. Floating-gate charging and discharging can be achieved by applying high drain pulses to the simple two-terminal device, yielding an on/off ratio of ~10^4 and paving the way for the design of nonvolatile memory devices based on vdW heterostructures.

3.3.2 | *Optoelectronic Transistors*

Optoelectronic synaptic transistors introduce optical signal modulation on the basis of traditional electrically controlled synapses, expanding application scenarios. They are mainly classified into two categories: photoelectric synergetic and all-optical types. Their core working mechanism largely relies on defect-state-mediated charge trapping and detrapping dynamics—photogenerated carriers are trapped by surface, interfacial, or bulk defects of materials under specific bias voltages and are slowly released after illumination ceases, resulting in delayed photocurrent decay. This constitutes the key physical foundation for emulating synaptic functions, and this mechanism has been widely applied in the design of optoelectronic artificial synapses and memristive devices. The performance comparisons in WBGS-based optoelectronic synaptic transistors are listed in Table 10.

GaN-based optoelectronic synaptic devices are a research focus, with a series of high-performance devices successfully developed: The light-stimulated synaptic transistor based on the AlGaN/GaN HEMT architecture regulates carrier

TABLE 8 | Performance comparisons in WBGS-based ferroelectric memristors.

Memristors	Power consumption (pJ)	Memory window	Forming voltage	Retention memory window (s)	Endurance (cycles)	On/off ratio	Refs.
$Ni/Al_{0.68}Sc_{0.32}N/Pt$	—	—	—	—	2×10^4	1.99	[143]
Ti/AuScAlN/GaN	—	—	—	3×10^5	10^4	60–210	[144]
ScAlN/n-GaN	—	—	—	$> 10^5$	$> 10^4$	10^4–10^5	[71]
n-GaN/i-GaN/AlScN	—	—	—	10^3	> 100	10^4	[111]
AlScN/p-i-n GaN	0.088	—	—	$> 10^4$	> 500	9.36×10^5	[6]
GaN/α-In_2Se_3 HEMT	—	—	—	~3.5	$> 5 \times 10^3$	~10^9	[145]
$CuInP_2S_6$/GaN HEMT	—	—	—	$> 3 \times 10^3$	$> 10^7$	~1.5×10^8	[146]

trapping/detrapping dynamics through spontaneous polarization, achieving EPSC responses that vary with optical pulse duration and spike number, thus robustly emulating synaptic functions. Yan et al. [156] adopted a 3T III-nitride MOSFET structure on a GaN-on-silicon platform, leveraging the defect charge storage effect at the AlGaN channel and AlGaN/SiO_2 interface to exhibit typical synaptic behaviors such as PPF and SRDP. Su et al. [158] proposed a dual-channel floating-gate artificial four-color synaptic device with a vertical WSe_2/3D GaN structure, using h-BN as the carrier barrier layer and multilayer graphene (MLG) as the charge storage layer. This device successfully emulates various basic synaptic behaviors, including STP, LTP, PPF, SNDP, SRDP, and STP-to-LTP transition, featuring excellent storage performance and broadband response capability. Hong et al. [159] integrated AlGaN/GaN HEMTs with 2D organic–inorganic halide perovskite (OIHP), realizing gate-tunable positive/negative photoresponses through the light-enhanced field effect, emulating functions such as EPSC, IPSC, and PPF, and achieving full-color perception. The Ni/Au/AlGaN Schottky-gate GaN-based optoelectronic transistor developed by Sun's group [160] eliminates the need for complex or unstable gate dielectrics, enabling self-powered detection, record-high responsivity in photoconductive mode, and optoelectronic synaptic behaviors in the subthreshold region. Its synaptic mechanism originates from the weak carrier depletion effect and PPC effect induced by subthreshold bias. Beyond the HEMT platform, Sun's group achieved a major breakthrough in GaN-based synaptic devices by introducing vdW metal contacts as an innovative strategy. Their pioneering work confirmed that the nondestructive nature of vdW interfaces can effectively suppress defect-related carrier recombination, simultaneously achieving high responsivity and PPC effect, thus opening up new possibilities for the design strategy of GaN-based synaptic devices [133].

In addition to GaN-based systems, wide-bandgap material-based optoelectronic synaptic devices have also yielded fruitful results: The 4H-SiC/organic semiconductor (PVK/P3HT) heterojunction synaptic transistor developed by Liu et al. [163] achieves non-volatility through heterojunction design and optical gating effect, with an energy consumption as low as 0.55 fJ per synaptic event. Its array successfully simulates the dynamic learning and forgetting processes of letter images. The diamond-based neuromorphic retinal perception system (NRPS) proposed by Liu et al. [26] introduces defects and doping states into diamond thin films through heteroepitaxial growth and silicon doping, realizing broadband spectral response, nonvolatile photocurrent, and wavelength sensitivity. It can simulate pupil constriction and image memory and further accomplish unknown color recognition and dynamic light-spot trajectory tracking, improving the UV image recognition accuracy from 67.5% to 81.7%. The nitrogen-doped ultrananocrystalline diamond thin-film optoelectronic system developed by Yao et al. [126] adopts an all-wireless architecture. When immersed in physiological media and irradiated with visible (595 nm) or near-infrared (808 nm) pulsed light, charge accumulation at the device–medium interface induces transient ionic displacement currents, thereby achieving electrical stimulation of neurons with high temporal resolution. Du et al. applied neuromorphic vision sensors to wide-area diamond quantum sensing, developing an efficient data processing protocol that significantly improves detection speed and precision, laying the foundation for the development of

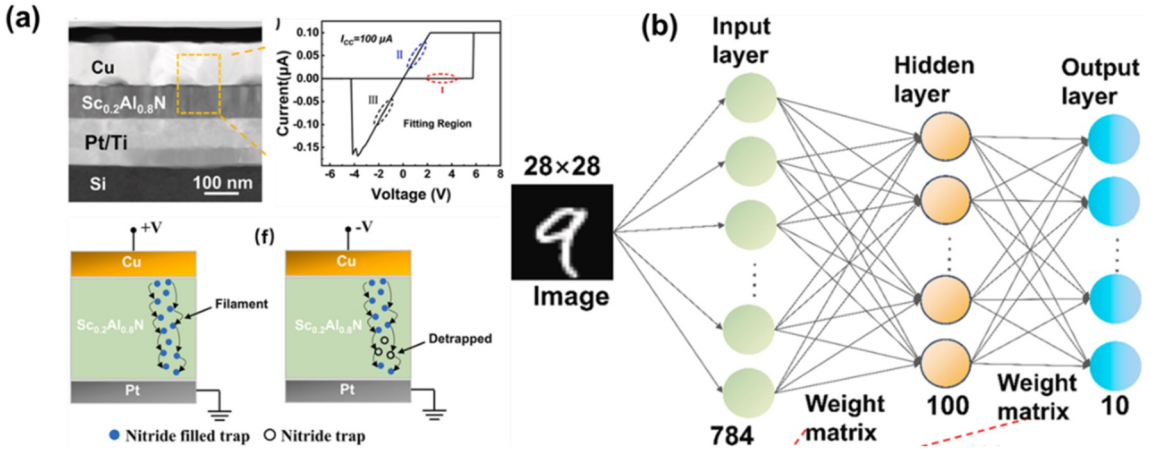

FIGURE 11 | (a) The $Cu/Sc_{0.2}Al_{0.8}N/Pt/Ti$ device and switching process during SET process. (b) Schematic diagram of memristor-based MLP neural networks. Reproduced with permission [72]. Copyright 2026, Materials Science in Semiconductor Processing.

TABLE 9 | Performance comparisons in WBGS-based electronic synaptic transistors.

Type	Materials	Device size	Stimulus signal (V)	Spike width (ms)	Per-spike energy consumption (pJ)	Synaptic/ neuronal functions	Refs.
TG	Semiconductor: AlGaN/GaN Top gate: Si_3N_4	—	0–10	1	—	EPSC PPF	[150]
SFG	Semiconductor: WSe_2/h-BN Semifloating gate: graphene	—	± 40	300	—	PPF	[151]
BG	Semiconductor: F-doped β-Ga_2O_3 Back gate: thin-film Au	L = 450 μm W = 500 μm	1	0.01	—	PPF LTP/LTD	[152]
BG	Semiconductor: In_2O_3 Back gate: Na-doped Ga_2O_3	L = 100 μm W = 1500 μm	0.5	20	1.07×10^2	EPSC/IPSC PPF/PPD STM/LTM SNDP LTP/LTD	[153]
Coplanar gates	Semiconductor: a-Ga_2O_3 Gate: sodium alginate (SA)	L = 10 nm W = 4 mm	2	—	—	Spatiotemporal logic encryption	[154]

Note: BG, TG, SG, SFG, and EG represent the bottom-gate configurations, top-gate configurations, side-gate configurations, semifloating-gate configurations, and extended-gate configurations, respectively.

intelligent quantum sensors. Through material integration innovation, structural optimization, and in-depth mechanism exploration, these studies comprehensively promote the development of optoelectronic synaptic devices toward low power consumption, multifunctionality, and high stability, providing diverse and efficient technical support for fields such as neuromorphic computing, artificial vision, and quantum sensing.

3.3.3 | *Ferroelectric Transistors*

Compared with memristors and optoelectronic synapses, ferroelectric synaptic transistors based on WBGSs remain relatively underexplored, yet they hold significant promise due to their nonvolatile polarization states, fast switching speed, and low energy consumption. To address this gap, Yang et al. [145] successfully demonstrated an artificial synapse by integrating a GaN-based MOS-HEMT with α-In_2Se_3, a ferroelectric semiconductor (Figure 12). The resulting GaN/α-In_2Se_3 vdW heterojunction is driven by a ferroelectrically coupled two-dimensional electron gas (2DEG), endowing the device with potential for high-frequency operation. Notably, the α-In_2Se_3 semiconductor itself exhibits a steep subthreshold swing and a high on/off ratio of approximately 10^{10}. A key structural design lies in the synergistic effect between the self-aligned α-In_2Se_3 layer and the gate electrode: This configuration suppresses in-plane polarization while enhancing the out-of-plane polarization of α-In_2Se_3, thereby

TABLE 10 | Performance comparisons in WBGS-based optoelectronic synaptic transistors.

Type	Materials	Device size (μm)	Stimulus signal	Spike width (ms)	Per-spike energy consumption (pJ)	Synaptic/ neuronal functions	Refs.
TG	GaN/AlN	—	365 nm	100, 200	—	EPSC PPF STM/LTM STDP	[9]
TG	Semiconductor: AlGaN/GaN Top gate: Ni/Au	$L_G = 1$ $L_{GS} = 2$ $L_{GD} = 3$ $W_G = 20$	405 nm 0.5 V	200	34.2	EPSC PPF STM/LTM	[155]
TG	Semiconductor: AlGaN/GaN Top gate: SiO_2	—	375 nm 0.2–5 mV	60	0.7×10^{-2}	PPF STM/LTM STP/LTP	[156]
TG	Semiconductor: AlGaN/GaN Top gate: SiN_x	$W = 100$ $L = 2$	375 nm 0.001 V	50	0.128	EPSC PPF STM/LTM	[9]
TG	Semiconductor: AlGaN/GaN Top gate: SiO_2	—	350 nm −5 V	100	—	EPSC PPF STP/LTP	[157]
FG	Semiconductor: WSe_2/GaN Floating gate: h-BN/MLG	—	310 nm −8 V	1	—	STP/LTP PPF SNDP SRDP	[158]
TG	Semiconductor: GaN/AlN Top gate: SiN_x	—	254 nm	50	—	PPF STM/LTM	[115]
TG	Semiconductor: AlGaN/GaN Top gate: Al/HfO_2/2D OIHP $(PEA)_2PbI_4$	$W = 200$ $L = 100$	532 nm 0.1 V	500	—	EPSC IPSC PPF	[159]
TG	Semiconductor: AlGaN/GaN Top gate: 2DEG	$W = 8.6$ $L = 3$	337, 254 nm 10 V	500	—	STM/LTM STP LTP EPSC	[160]
TG	Semiconductor: AlGaN/GaN Top gate: Ti/Au	—	310, 375, 405 nm 27.1–673 W/m^2 V_{gs}: −6 to 6 V	10, 20, 30	—	EPSC PPF STM to LTM	[161]
BG	Semiconductor: Ga_2O_3/MoS_2 Back gate: p-Si	—	532 nm $V_{gs} = -25$ V	1000	—	STP/LTP PPF STM/LTM	[162]
BG	Semiconductor: Si-doped diamond Back gate: Si/SiO_2	—	From DUV to NIR 222–1064 nm 10 mV	10	222 nm: 0.506 532 nm: 2.3×10^{-3}	EPSC PPF STDP STM/LTM	[26]

achieving a steep subthreshold swing of 10 mV/dec and a significant hysteresis of 2 V. Leveraging the STP characteristics of the fabricated ferroelectric HEMT, the researchers further implemented reservoir computing (RC) for image classification tasks. This work highlights the GaN/α-In_2Se_3 ferroelectric HEMT as a viable pathway toward ultrafast neuromorphic computing, offering a promising combination of wide-bandgap material advantages, ferroelectric modulation capabilities, and synaptic functionality for next-generation brain-inspired systems.

3.4 | Neuronal Devices

Artificial neuron devices are as indispensable as synaptic elements for constructing complete neuromorphic hardware

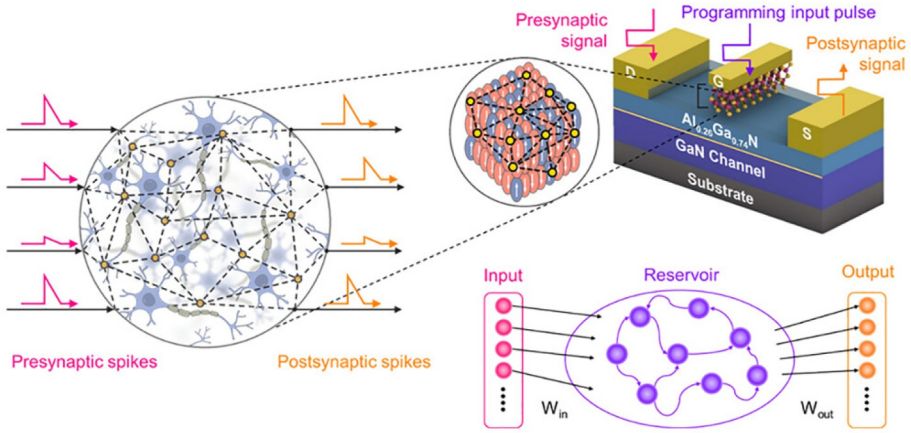

FIGURE 12 | Presynaptic and postsynaptic schematics of the emulated neuron system in RC. Reproduced with permission [145]. Copyright 2023, ACS Nano.

systems. Although numerous mathematical neuron models have been proposed over the past decades, software-based implementations relying on the numerical solution of large sets of differential equations are inherently limited by high computational complexity, substantial energy consumption, and inefficient data movement. In contrast, hardware-implemented artificial neurons directly exploit device-level physical dynamics to emulate neuronal behaviors, offering significant advantages in speed, energy efficiency, and scalability [164]. From a device perspective, artificial neurons based on volatile switching materials are especially well suited to emulate biological neuronal dynamics. In such systems, RS thresholds act as spike-triggering conditions, whereas intrinsic volatility enables spontaneous relaxation, giving rise to oscillatory or pulsed output waveforms analogous to biological spike trains [165]. These dynamic behaviors support a wide range of neural network architectures. For instance, coupled neuronal oscillators form the basis of optical neural networks (ONNs), whereas leaky integrate-and-fire (LIF) neurons—characterized by temporal integration, membrane potential decay, and threshold firing—are fundamental building blocks of spiking neural networks (SNNs) [166–169]. Moreover, the intrinsic stochasticity associated with complex switching physics enables probabilistic spiking behavior, supporting advanced computing paradigms such as Boltzmann machines, Bayesian networks, and pulse-coupled neural networks [170].

A typical biological neuron consists of dendrites, a soma, and an axon (Figure 13). Key neuronal features include spatiotemporal integration of presynaptic spike trains, short-term memory effects in membrane potential evolution, probabilistic sigmoid-like activation at the axon hillock, and ion-channel-mediated signal transduction across the membrane. Together, these properties allow neurons to aggregate and encode temporally correlated inputs, perform noise-tolerant information processing, and generate rule-based output spike sequences—functional principles that guide the design of artificial neuron devices.

To date, reports on neuron devices based on WBGSs remain relatively limited. Yan's group [172] demonstrated a multilayer Al/AlN/Ag/AlN/Pt thin-film device exhibiting threshold switching behavior with a fast response time of ~50 ns and ultralow leakage current. When incorporated into a LIF circuit, this TS device successfully emulated key neuronal functions, including threshold-triggered spiking, all-or-nothing firing, intensity-dependent spiking frequency, and frequency modulation, surpassing the performance of many earlier artificial neuron implementations. The underlying switching mechanism is attributed to the synergistic migration of nitrogen vacancies and silver filaments, highlighting the potential of nitride-based volatile devices for artificial neuron hardware. In parallel, optoelectronic neuron devices based on WBG materials have emerged as promising biointerfaces. Yao et al. [126] developed an optically controlled, nonhereditary neural stimulation system using nitrogen-doped ultrananocrystalline diamond thin films grown directly on silicon substrates. This all-wireless platform operates under visible (595 nm) or near-infrared (808 nm) pulsed illumination: Charge accumulation at the device–electrolyte interface induces transient ionic displacement currents, enabling high-temporal-resolution electrical stimulation of neurons. The system was validated through photoelectric stimulation of degenerated rat retinas, achieving a photoresponsivity of 7.5 $mA \cdot W^{-1}$ under illumination conditions well below ocular safety limits. This work pioneers the use of diamond-based optoelectronic devices capable of generating sufficient photocurrent for direct neuronal activation, underscoring the potential of WBGSs in biointegrated neuromorphic and neuroprosthetic applications.

4 | Integration, Benchmarking, and Applications

4.1 | Integration With CMOS and Power Electronics

The integration of neuromorphic functionalities with conventional electronics constitutes a central development direction for next-generation intelligent electronic systems. In this context, WBGSs have emerged as particularly attractive platforms, owing to their intrinsic material advantages and compatibility with mature semiconductor manufacturing processes. Early efforts to realize neuromorphic behavior in GaN devices focused on emulating human sensory and perception functions. Representative demonstrations include pressure-sensitive GaN HEMTs, in which external mechanical stimuli modulate the 2DEG density and thereby enable real-time regulation of output power, as well as multifunctional devices that integrate pressure sensing and

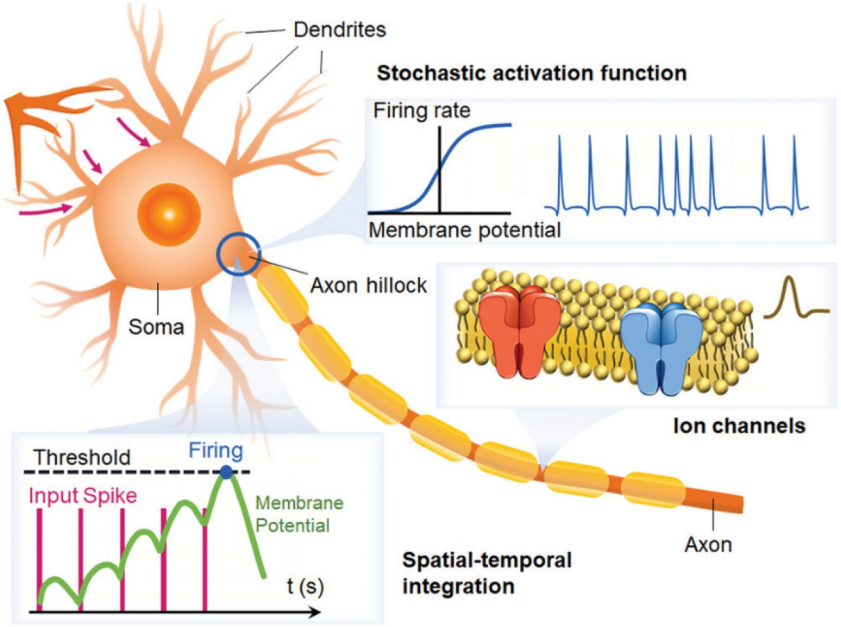

FIGURE 13 | Schematic diagram of a typical neuron. A typical neuron consists of a cell body, axon, and dendrites. The book highlights several key neuronal features: spatiotemporal integration of incoming spike trains, short-term memory effects on membrane potential (lower-left diagram), probabilistic sigmoid activation functions in axon hillocks (upper-right diagram), and ion channels on the cell membrane (lower-right diagram). These properties enable neurons to collect information inputs from multiple synapses, analyze and encode temporal correlations, process information in a fault-tolerant manner, and generate output spike trains (action potentials) according to a set of rules. Reproduced with permission [171]. Copyright 2023, Advanced Materials.

synaptic plasticity by exploiting the strong piezoelectric response of GaN NWs [173]. Although GaN-on-Si heteroepitaxial growth inevitably introduces crystalline defects—such as threading dislocations, stacking faults, and dangling bonds arising from lattice mismatch—these imperfections have been strategically repurposed as three-dimensional charge storage centers for neuromorphic operation. Moreover, the incorporation of piezoelectric, optical, or ferroelectric functionalities has further enriched the neuromorphic response space. Importantly, many of these GaN-based neuromorphic devices are compatible with CMOS fabrication workflows, underscoring their strong potential for large-scale integration and commercialization.

A growing body of work has demonstrated high-performance WBG neuromorphic devices with explicit CMOS and power-electronics relevance. Li et al. [150] exploited dendritic dislocations in GaN HEMTs as 3D charge storage sites to emulate neuron-like information processing and synaptic transmission. Notably, these devices were fabricated on 6-inch GaN-on-Si wafers with a yield as high as 95%, highlighting their manufacturability (Figure 14). Sun et al. [161] reported a GaN-based optoelectronic integrated chip comprising a series-connected InGaN/GaN multiple-quantum-well (MQW) LED and a GaN optoelectronic synaptic MOSFET, enabling multimodal functionalities such as self-powered detection, wavelength-selective response, and light-emitting synapses. In the ferroelectric domain, Pan et al. [174] for the first time grew ferroelectric $Al_{0.8}Sc_{0.2}N$ thin films on CMOS-compatible tungsten substrates, with the resulting memristors exhibiting nanosecond-scale switching speed and excellent retention; the ANN constructed based on these memristors achieved a 93.9% recognition accuracy on the MNIST dataset. Similarly, Wang et al. [175] optimized $Al_{0.77}Sc_{0.23}N$ thin films via magnetron sputtering and demonstrated Pd/AlScN/TiN/Si memristors capable of emulating diverse synaptic plasticity behaviors, and the corresponding STDP circuit was successfully validated in unmanned aerial vehicle (UAV) flight marker recognition tasks.

Beyond individual devices, complementary integration strategies and emerging materials have further expanded the scope of WBG-based neuromorphic systems. Ren et al. [176] developed a CMOS-compatible photonic integrated circuit platform based on AlN/Si waveguides for near-sensor edge computing. By combining the electro-optic response of AlN microring resonators for photonic feature extraction with silicon-based thermo-optic Mach–Zehnder interferometers for neural network computation, this system achieved gesture and gait recognition accuracies exceeding 96%, with sub-10-ns latency and sub-picojoule energy consumption (< 0.34 pJ). Zhu et al. [177] integrated h-BN memristors into the BEOL interconnects of CMOS-compatible silicon chips, realizing high-precision current modulation and long cycling endurance; the resulting 1T1M crossbar arrays demonstrated effective power reduction. In parallel, Kapur et al. [89] developed memristors based on BEOL-compatible SiC, fabricating Cu/SiC/W stacked devices via CVD. These devices exhibited excellent binary RS with compliance-free and self-rectifying characteristics, offering advantages for high-density 3D crossbar storage architectures and potential for wafer-scale fabrication.

4.2 | Application Scenarios

Leveraging their inherent advantages of wide bandgaps, high thermal stability, tunable defect dynamics, and versatile

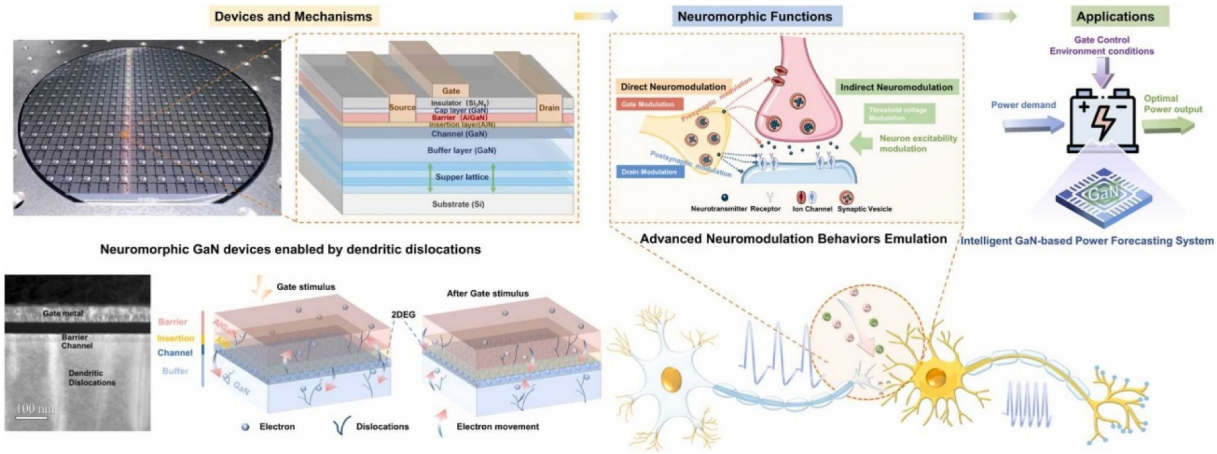

FIGURE 14 | The processing function of neurons emulated by a GaN device. Reproduced with permission [150]. Copyright 2024, Nano Energy.

optoelectronic properties, WBGSs have spawned diverse high-performance neuromorphic devices. These devices have penetrated key application scenarios of neuromorphic computing, spanning fundamental logic operations, secure signal encryption, brain-inspired visual perception and processing, efficient RC, and extreme-environment high-temperature image learning. The following sections detail representative device architectures, core working mechanisms, and performance benchmarks for each application field, highlighting the unique value of WBGSs in advancing intelligent systems.

4.2.1 | *Logic Operation*

With the rapid advancement of in-memory computing and neuromorphic systems, there is an urgent demand for multifunctional devices that integrate high-performance storage, logic operations, and synaptic plasticity—capabilities critical to overcoming the von Neumann bottleneck. WBGSs have emerged as promising candidates for such applications, leveraging their inherent advantages of ultralow leakage, high breakdown fields, and tunable defect/interface dynamics.

He et al. [98] constructed a vertical Ag/β-Ga_2O_3/Pt memristor on high-crystalline-quality β-Ga_2O_3 thin films via lattice epitaxy engineering and sacrificial-layer-assisted transfer (Figure 15a). The β-Ga_2O_3-based device exhibited exceptional performance, including an on/off ratio exceeding 10^8, low programming/reset voltages (0.13 V/−0.11 V), ultralow programming current (10^{-10} A), long data retention ($> 4 \times 10^4$ s), and excellent subthreshold characteristics (~0.47 mV·dec^{-1}). Tunable I_{cc} enabled the coexistence of volatile and nonvolatile switching modes. Electrical characterizations combined with first-principles calculations revealed that the diverse RS behaviors are dominated by Ag ion migration. A reconfigurable nonvolatile XOR logic-gate circuit based on this β-Ga_2O_3 memristor was designed and simulated, enabling image encryption/decryption and edge detection functions. This work not only validated the feasibility of lattice-engineered high-quality β-Ga_2O_3 thin films for advanced memristor fabrication but also expanded their applications into digital logic and reconfigurable image processing. Cui et al. [129] proposed an amorphous wide-bandgap Ga_2O_3 optoelectronic synaptic memristor, achieving 3-bit data storage by modulating I_{cc} and variable ultraviolet (UV 254 nm) light intensity (Figure 15b). By utilizing voltage polarity and UV light as input signals, the device realized "AND" and "OR" logic-gate functions in memristor-aided logic (MAGIC). It also exhibited highly stable synaptic characteristics, including PPF, spike-intensity-dependent plasticity (SIDP), spike-number-dependent plasticity (SNDP), STDP, spike-frequency-dependent plasticity (SFDP), and learning-experience behaviors. When integrated into an ANN, the Ag/Ga_2O_3/Pt memristor simulated light-pulse potentiation and electric pulse depression with a high pattern accuracy of 90.7%, making this multifunctional single memristive unit a promising candidate for optoelectronic memory, neuromorphic computing, and artificial visual perception applications. Xie et al. [111] adopted an n-GaN/i-GaN/AlScN heterojunction Schottky diode structure, achieving an on/off ratio of ~10^4 in both electrical and optoelectronic modes, with reliable resistance-state resetting, writing, and long-term retention (Figure 15c). In the electrical mode, resistance-state changes originate from ferroelectric polarization reversal in the AlScN layer of the heterostructure, which modulates the device's depletion region width and electron transport barrier height. In the optoelectronic mode, the storage window can be tuned by light intensity via the photoconductive effect of the i-GaN layer and light-induced reduction of the electron transport barrier, thereby adjusting the partial bias applied to the AlScN layer. Based on this device, the implication (IMP) truth table and logic "FALSE" state were successfully reproduced, demonstrating its significant potential in in-sensor computing and memory-computing-integrated systems.

4.2.2 | *Signal Encryption*

Currently, signal encryption research based on WBGSs primarily focuses on memristors and optoelectronic devices, leveraging the unique electrical, optical, and environmental stability of WBG materials to address emerging security challenges in hardware systems. Li et al. [154] developed vertical short-channel Ga_2O_3 TFTs to mitigate security threats in critical hardware components (Figure 16a). Featuring an ultrashort channel length of ~10 nm enabled by the vertical structural design, the device operates stably at a low voltage of 2 V with a reasonable on/off ratio of 10^3. More importantly, it achieves spatiotemporal logic encryption by regulating ion coupling paths, whereas its AND-gate logic decryption function can only be activated by reducing the gate-channel spacing, enhancing hardware security

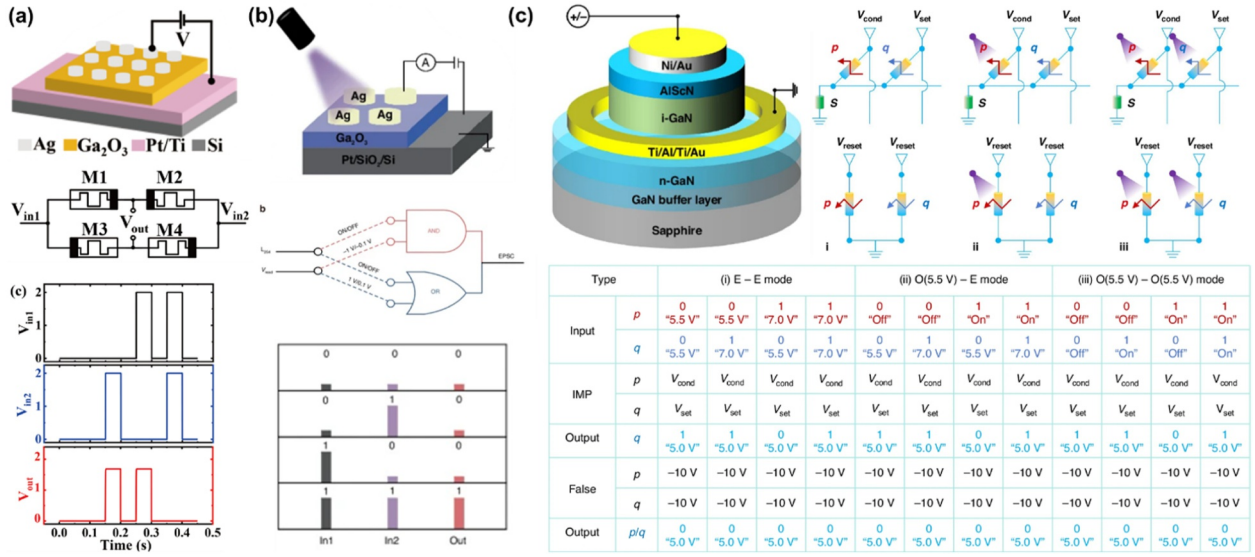

Type		(i) E – E mode				(ii) O(5.5 V) – E mode				(iii) O(5.5 V) – O(5.5 V) mode			
Input	p	0 "5.5 V"	0 "5.5 V"	1 "7.0 V"	1 "7.0 V"	0 "Off"	0 "Off"	1 "On"	1 "On"	0 "Off"	0 "Off"	1 "On"	1 "On"
	q	0 "5.5 V"	1 "7.0 V"	0 "5.5 V"	1 "7.0 V"	0 "5.5 V"	1 "7.0 V"	0 "5.5 V"	1 "7.0 V"	0 "Off"	1 "On"	0 "Off"	1 "On"
IMP	p	V_{cond}	V_{cond}	V_{cond}	V_{cond}	V_{cond}	V_{cond}	V_{cond}	V_{cond}	V_{cond}	V_{cond}	V_{cond}	V_{cond}
	q	V_{set}	V_{set}	V_{set}	V_{set}	V_{set}	V_{set}	V_{set}	V_{set}	V_{set}	V_{set}	V_{set}	V_{set}
Output	q	1 "5.0 V"	1 "5.0 V"	0 "5.0 V"	1 "5.0 V"	1 "5.0 V"	1 "5.0 V"	0 "5.0 V"	1 "5.0 V"	1 "5.0 V"	1 "5.0 V"	0 "5.0 V"	1 "5.0 V"
False	p	−10 V	−10 V	−10 V	−10 V	−10 V	−10 V	−10 V	−10 V	−10 V	−10 V	−10 V	−10 V
	q	−10 V	−10 V	−10 V	−10 V	−10 V	−10 V	−10 V	−10 V	−10 V	−10 V	−10 V	−10 V
Output	p/q	0 "5.0 V"	0 "5.0 V"	0 "5.0 V"	0 "5.0 V"	0 "5.0 V"	0 "5.0 V"	0 "5.0 V"	0 "5.0 V"	0 "5.0 V"	0 "5.0 V"	0 "5.0 V"	0 "5.0 V"

FIGURE 15 | (a) β-Ga_2O_3-based memristor circuit for image encryption. Reproduced with permission [98]. Copyright 2026, Science China Materials. (b) Architecture and performance of a Ga_2O_3-based photoelectric synaptic memristor for logic gates. Reproduced with permission [129]. Copyright 2025, Light: Science & Applications. (c) The electro-optic duplex memristor on a GaN/AlScN heterostructure-based Schottky diode. Reproduced with permission [111]. Copyright 2024, Light: Science & Applications.

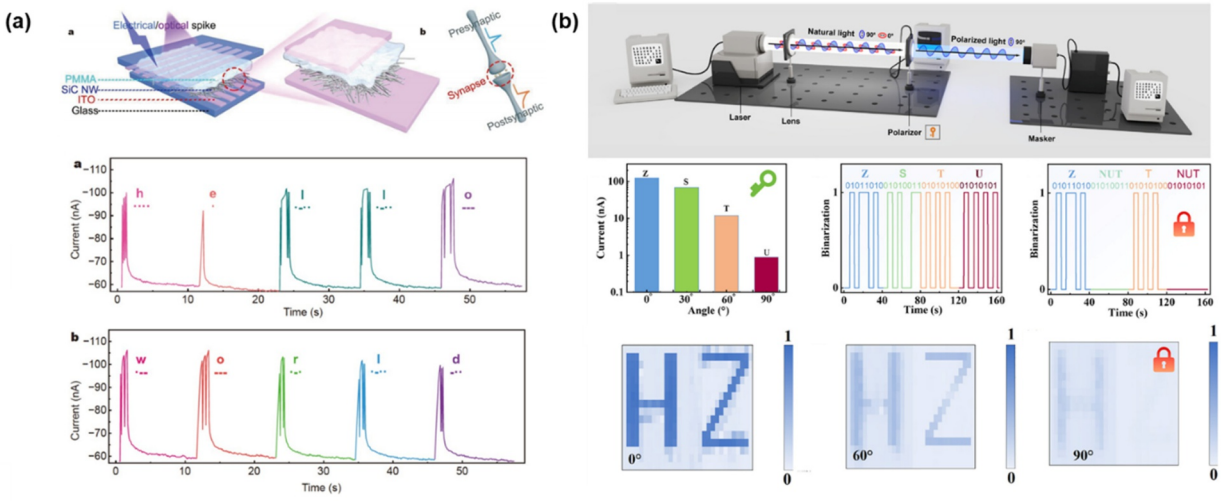

FIGURE 16 | (a) 365 nm light-triggered EPSC amplitudes of the SiC NW artificial synaptic device under International Morse code stimulation. Reproduced with permission [178]. Copyright 2023, Science China Materials. (b) Polarized light encryption information transmission system. Reproduced with permission [125]. Copyright 2025, Advanced Optical Materials.

through structural design. Shen et al. [178] demonstrated the capability of 3C-SiC NW synaptic devices to distinguish Morse code characters. Their findings revealed that these devices respond to optical signals representing International Morse code, with each character triggering a distinct EPSC amplitude response. Individual characters can be identified by analyzing the sum and endpoints of EPSC amplitude peaks; comparative analysis of SUM and END patterns confirmed accurate recognition of each Morse code, facilitating encrypted data transmission and identification. Liu et al. [140] exploited the significant optical gating effect induced by efficient separation of photogenerated carriers at the p-n 4H-SiC homojunction interface, enabling robust light-stimulated synaptic behaviors in the device without encapsulation in ambient air at 350°C. Through array integration, the devices successfully realized information encryption and image learning/memory functions at 350°C, highlighting their potential for high-temperature secure computing scenarios. As a fundamental degree of freedom of light, optical polarization provides a powerful dimension to enhance information capacity in optoelectronic systems. By encoding data into polarization states (e.g., linear, circular, or elliptical polarization), a single light beam can transmit multiplexed information channels, offering a superior alternative to traditional intensity-based signals. This unique property has driven advanced applications in optoelectronics, including reconfigurable photonic logic gates based on polarization-sensitive devices, as well as advancements in secure communications where polarization states serve as cryptographic keys for

optical information encryption and decryption. Zhao et al. [125] obtained high-quality β-Ga_2O_3 MWs from bulk single crystals via simple mechanical exfoliation (Figure 16b). Utilizing the inherent polarization-sensitive anisotropy of β-Ga_2O_3, a lens-free polarized photodetector was realized, exhibiting solar-blind operation insensitive to visible-light backgrounds, an ultrahigh polarization ratio of 137 at 254 nm, and excellent reproducibility. Leveraging this exceptional polarization sensitivity, the study achieved on-chip reconfigurable OR/AND logic operations via polarization modulation and realized optical encryption based on polarization-encoded signals.

4.2.3 | *Visual Perception and Processing*

Humans acquire over 80% of information about the external environment through the visual system. Efficiently emulating the perceptual capabilities and information processing mechanisms of the human visual system has long been a core goal of bionic research. Currently, WBGS-based neuromorphic devices exhibit remarkable potential in brain-inspired visual perception and processing. In terms of electronic devices, the sodium-doped Ga_2O_3 three-terminal EGST demonstrates high-accuracy pattern recognition capabilities when integrated into ANNs. For optoelectronic devices, all types of WBGSs mentioned herein have been applied in image recognition. The current trend is to fabricate device arrays to improve recognition accuracy, thereby enabling the recognition of complex and dynamic images. Sun's group [132] first reported a p-GaN/n-AlGaN/n-GaN nanowire diode grown on a Si substrate (Figure 17a). This embedded electron reservoir architecture enables sophisticated regulation of charge trapping and detrapping dynamics, breaking the operational limitations of conventional p-n junction paradigms. It endows the system with bias-modulable optoelectronic characteristics, including tunable photoresponsivity reaching 10.45 mA/W, photonic synaptic behavior with a PPF as high as 122%, and optical memory performance featuring eight discrete linear conductance states. Furthermore, the three-in-one diode array is capable of constructing compact, energy-efficient image-sensing hardware. Zhang et al. [162] successfully fabricated a Ga_2O_3/MoS_2 heterojunction optoelectronic device by stacking n-type Ga_2O_3 and n-type MoS_2 layers (Figure 17b). The device achieves a rectification ratio of $\approx 10^5$, an on/off ratio of $\approx 10^8$, a high detectivity of 1.34×10^9 Jones, and a high responsivity of 28.92 mA/W. More importantly, this heterojunction device demonstrates potential for integrating sensing and storage functions, making it suitable for use as an artificial neuromorphic synapse. By synergistically regulating the optical switching state and gate voltage, the device exhibits information processing capabilities as the optoelectronic logic gate "AND."

4.2.4 | *Reservoir Computing*

RC, a machine learning framework, has garnered significant attention for its ability to circumvent error accumulation in traditional recurrent networks while reducing hardware costs. Within neuromorphic architectures, RC is renowned for its suitability in processing time-series and high-dimensional data, featuring a three-layer structure: an input layer, an untrained fixed reservoir layer that nonlinearly maps inputs to a high-dimensional space, and a trainable linear readout layer for high-dimensional state classification. RC systems based on spintronic oscillators, photonic modules, nanonetworks, and memristors have been successfully demonstrated. Recently, an in-sensor RC system based on GaN HEMTs was proposed to maximize the performance of neuromorphic computing for in situ processing of large datasets in hardware. Jiang et al. [179] experimentally validated an in-sensor RC system for intelligent gas sensing, where the core GaN HEMT exhibits nonlinear dynamic channel conductivity that varies with gas concentration. This device follows gate-modulated nonlinear dynamics with a fading memory effect, physically encoding each 4-bit sequence

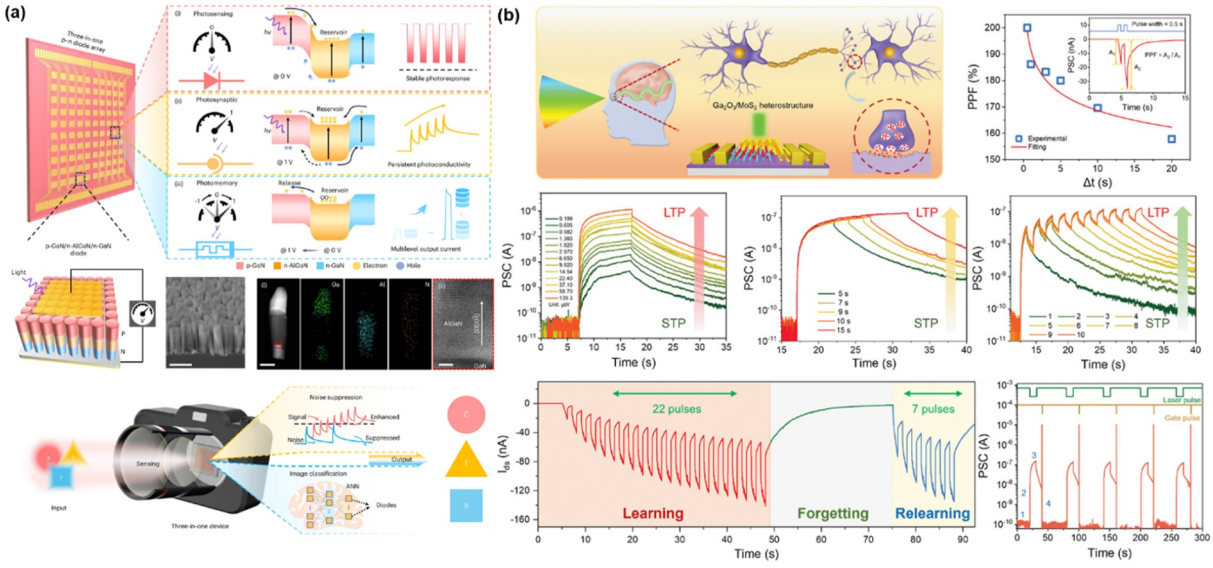

FIGURE 17 | (a) Three-in-one image sensor based on a multifunctional p-GaN/n-AlGaN/n-GaN nanowire diode architecture. Reproduced with permission [132]. Copyright 2026, Nature Electronics. (b) Neuron/synaptic functions of the Ga_2O_3/MoS_2 heterostructure device as a neuromorphic vision sensor. Reproduced with permission [162]. Copyright 2024, Advanced Functional Materials.

into a unique and distinguishable ID. A single-layer fully connected neural network (FCNN) leverages these reservoir states (IDs) to learn gas pattern classification. Guo et al. [180] demonstrated a BEOL-compatible SiC-based memristor that exhibits short-term memory properties and can encode temporal signals. A physical RC system centered on this memristor was constructed and experimentally validated for pattern recognition tasks (Figure 18). After training, the RC system achieved 100% accuracy in classifying 0–9 digit patterns and demonstrated excellent robustness against noisy pixels.

4.2.5 | *High-Temperature Image Learning and Memory*

Most neuromorphic devices currently operate solely at room temperature, limiting their deployment in extreme-environment computing scenarios such as aerospace, automotive, geothermal, and oil and gas industries. For instance, high-temperature image preprocessors in UAVs could capture close-range imagery near volcanoes or wildfires if capable of withstanding extreme temperatures while also reducing image computation loads. Developing neuromorphic devices for high-temperature front-end data preprocessing thus helps expand application boundaries.

WBGSs inherently tolerate higher temperatures: Ga_2O_3 has shown potential in power devices with a breakdown voltage of 8.32 kV, and recently, in-memory sensing systems based on Ga_2O_3 synaptic memristor arrays were demonstrated for intelligent fingerprint recognition. However, amorphous Ga_2O_3 crystallizes at elevated temperatures, restricting high-temperature applications. Benefiting from both high-temperature resistance and polarization properties, ε-Ga_2O_3 emerges as a promising candidate. As shown in Figure 19a, Lin et al. [181] fabricated a high-temperature image preprocessor using ε-Ga_2O_3 optical synapses: High-quality ε-Ga_2O_3 thin films were epitaxially grown via mist chemical vapor deposition, and a large photodetector array (152 devices) was constructed, featuring pA-level dark current, 5–6 orders of magnitude photoswitching ratio, and high uniformity. Notably, the devices exhibited significant photoinduced compression effects and synaptic behaviors, which improved at high temperatures, originating from the competitive mechanism between carrier trapping/detrapping and mobility fluctuation. Based on this, high-temperature image compression was achieved: 4 × 4 pixel images were compressed to 4 × 1 vectors at 650 K, reducing data volume for subsequent recognition, with 100% accuracy after 32 training epochs at 650 K.

Other WBG materials have also been explored for high-temperature optoelectronic synapses: Xiaodong Pi's group [182] developed 4H-SiC-based devices, where a 3 × 3 array-based neural network showed stable performance across temperatures, realizing multiple optoelectronic synaptic functions up to 600 K (Figure 19b). A 4H-SiC p-n homojunction synaptic device achieved superior light-stimulated synaptic behaviors in ambient air at 350°C (without encapsulation) due to efficient separation of photogenerated carriers at the homojunction interface, enabling information encryption and image learning/memory simulations at 350°C [140]. Its array achieved 95% accuracy in MNIST handwritten digit recognition via ANN simulation. Shen et al. [183] reported high-temperature brain-inspired synaptic devices based on SiC@NiO core–shell NW network optoelectronic memristors (NNOMs), which exhibited short/long-term synaptic plasticity and modulatory plasticity under electrical/optical stimulation, with stable short/long-term memory and "learning-forgetting-relearning" functions at room temperature and 200°C. A 5 × 3 optoelectronic synaptic array maintained stable visual memory at 200°C, suitable for artificial visual

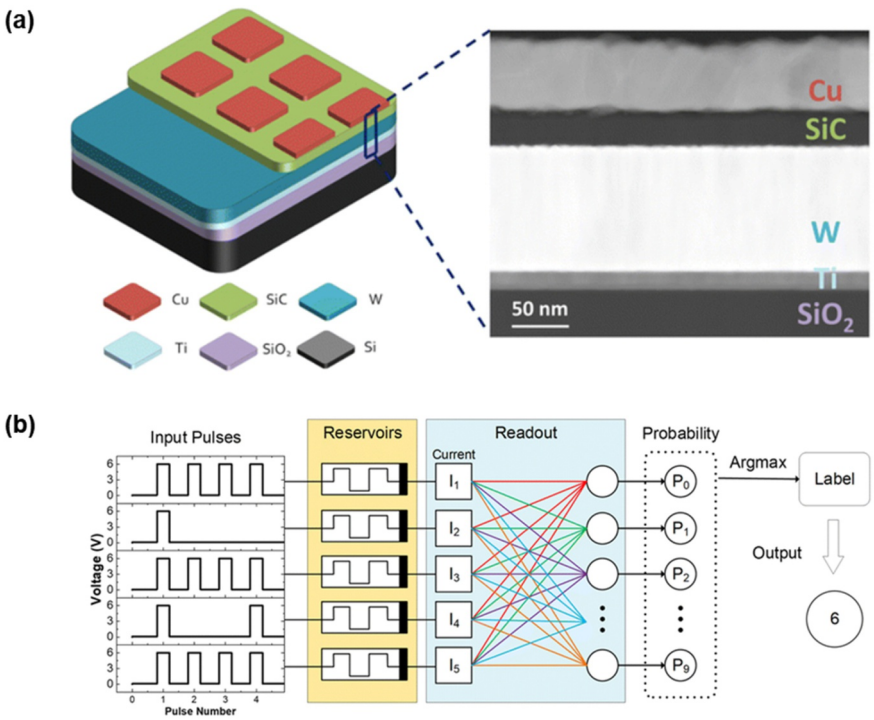

FIGURE 18 | (a) Schematic of the Cu/SiC/W memristor structure. (b) Schematic representation of the physical RC system including the inputs (pulse streams), the SiC memristor reservoir, and the readout network. Reproduced with permission [180]. Copyright 2023, Materials Advances.

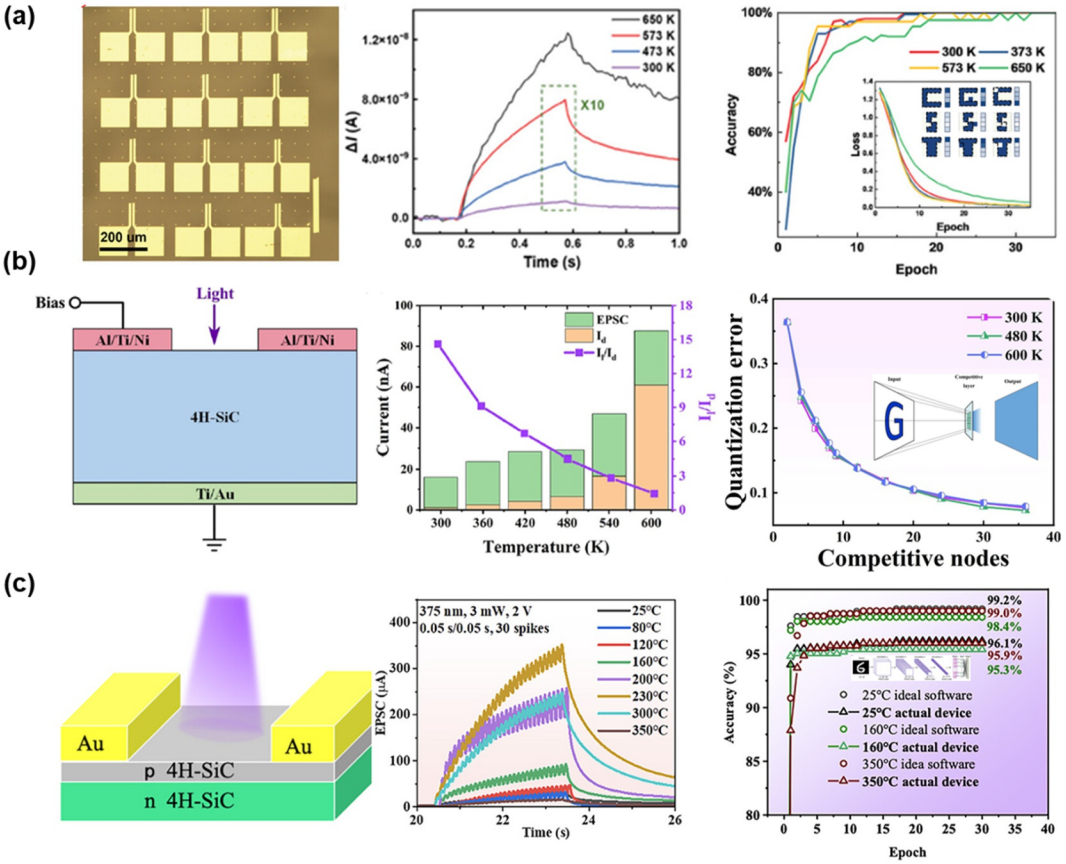

FIGURE 19 | (a) Photodetectors based on ε-Ga_2O_3. Reproduced with permission [181]. Copyright 2024, Advanced Physics Research. (b) 4H-SiC synaptic device. Reproduced with permission [182]. Copyright 2025, Science China Information Sciences. (c) High-temperature-resistant synaptic devices based on the p-n 4H-SiC homojunctions. Reproduced with permission [140]. Copyright 2025, Small.

system development. These WBG-based devices demonstrate significant potential as high-temperature optoelectronic synapses, expanding the operating temperature range of optoelectronic neuromorphic computing systems.

5 | Challenges and Future Perspectives

Despite the rapid progress of WBGS-based neuromorphic devices, several critical challenges must be addressed before these materials can be translated into large-scale, reliable, and application-ready neuromorphic systems (Figure 20).

Material uniformity and defect control: Defects play a dual role in WBG neuromorphic devices. Although vacancies, dislocations, and interface states are often deliberately exploited to enable analog RS and synaptic plasticity, their stochastic nature also introduces device-to-device variability and cycle-to-cycle instability. This challenge is particularly pronounced in materials such as GaN and Ga_2O_3, where dislocations, oxygen vacancies, and interface traps are strongly dependent on growth conditions and substrate choice. Future research should move from defect utilization toward defect-by-design strategies, in which defect types, spatial distributions, and densities are precisely engineered through advanced epitaxial growth, doping control, and post-processing techniques. Establishing clear correlations between defect physics and neuromorphic functionality will be essential for improving uniformity and reproducibility.

Device reliability and energy efficiency: Although WBG materials inherently offer high breakdown fields and thermal robustness, long-term reliability under repeated programming cycles remains a concern, especially for defect- or ion-migration-based devices. Issues such as conductance drift, retention degradation, and switching endurance must be systematically evaluated under realistic operating conditions, including elevated temperatures and high electric fields. In addition, some WBG neuromorphic devices still operate at relatively high voltages compared with biological synapses or emerging low-power oxide systems. Reducing operating voltage and energy consumption through interface engineering, polarization-assisted modulation, and ferroelectric integration represents an important direction for future device optimization.

Scalability and integration compatibility: Scalable integration is a key bottleneck for WBG neuromorphic hardware. Although GaN and SiC benefit from relatively mature wafer-scale growth and CMOS compatibility, other materials such as Ga_2O_3 and diamond still face challenges related to thermal management, substrate availability, and process standardization. Ga_2O_3-based memristors have exhibited favorable compatibility with CMOS and 3D integration in preliminary attempts, yet such integration technology remains in the early developmental stage. Thus, the integration of neuromorphic functionality with existing electronic platforms—particularly BEOL compatibility, three-dimensional crossbar architectures, and hybrid CMOS-WBG

FIGURE 20 | Future perspectives for WBGS-based neuromorphic computing. The authors own the copyright.

systems—requires further development. Advancing low-temperature fabrication processes and heterogeneous integration schemes will be crucial for enabling high-density neuromorphic circuits.

Algorithm-hardware codesign: A lack of standardized benchmarking metrics makes it difficult to fairly compare WBG neuromorphic devices with conventional material platforms. Parameters such as linearity, symmetry, dynamic range, energy per synaptic event, temperature stability, and noise tolerance should be evaluated in a unified manner. Furthermore, most demonstrations to date rely on conventional neural network models that are not optimized for the intrinsic properties of WBG devices. Developing algorithm-hardware codesign strategies—such as SNNs and RC architectures tailored to nonlinear switching, volatility, or optoelectronic coupling—will be essential to fully exploit the unique advantages of WBG materials.

Multifunctional and extreme-environment intelligence: Looking forward, WBGSs offer distinctive opportunities that extend beyond conventional neuromorphic computing. Their robustness under high-temperature, high-radiation, and high-electric-field environments positions them as ideal candidates for intelligent systems in aerospace, nuclear energy, and geothermal applications. In addition, the strong optoelectronic and polarization properties of WBG materials enable natural integration of sensing, memory, and computing within a single device, opening pathways toward in-sensor and edge intelligence. The convergence of neuromorphic computing with power electronics, photonics, and harsh-environment electronics represents a particularly promising direction for future research.

In summary, WBGSs are transitioning from passive electronic materials to active enablers of neuromorphic computing. Continued advances in defect engineering, interface design, scalable integration, and algorithm-aware device development are expected to unlock their full potential. As these challenges are progressively addressed, WBG semiconductor-based neuromorphic computing is poised to complement and extend existing technologies, enabling robust, efficient, and multifunctional intelligent systems operating beyond the limits of conventional material platforms.

6 | Conclusions

WBGSs, including GaN, AlN, BN, SiC, Ga_2O_3, and diamond, have emerged as a powerful material platform for neuromorphic computing beyond the limitations of conventional silicon-based systems. Their intrinsic properties—large bandgaps, high breakdown fields, excellent thermal stability, rich defect physics, and strong polarization effects—enable robust, energy-efficient, and multifunctional neuromorphic devices capable of operating under extreme electrical, thermal, and radiation environments. This review has systematically summarized recent advances in WBG-based neuromorphic computing from material fundamentals to device architectures, physical mechanisms, and application demonstrations.

From a material and device perspective, III–V nitrides enable polarization-modulated and optoelectronic synaptic functionalities, SiC supports high-temperature and radiation-hard neuromorphic systems, Ga_2O_3 offers ultrahigh breakdown fields with defect-tunable memristive behavior, and diamond provides superior thermal management and low-noise characteristics for photonic neuromorphic applications. Building on these material advantages, diverse neuromorphic device architectures—including memristors, synaptic transistors, and artificial neurons—have been realized through defect- and interface-

mediated transport, polarization-controlled carrier modulation, and photoelectrothermal coupling, achieving key synaptic and neuronal functions with performance metrics that rival or exceed those of biological and conventional counterparts. At the system level, WBG neuromorphic devices demonstrate favorable CMOS compatibility, enabling BEOL integration and 3D crossbar architectures. Their successful deployment in logic operations, visual perception, RC, and high-temperature image learning highlights particular strengths in edge intelligence and extreme-environment applications where traditional technologies face fundamental limitations. These advances underscore the unique potential of WBG materials to merge sensing, memory, and computing within robust and compact hardware platforms.

Looking forward, challenges related to defect-induced variability, long-term reliability, large-scale integration, and algorithm-hardware codesign remain to be addressed. Continued progress in defect-by-design strategies, multifunctional device innovation, and neuromorphic architectures tailored to WBG material characteristics is expected to unlock the full potential of this material class. With ongoing advances in material engineering and system integration, WBG semiconductor-based neuromorphic computing is poised to become a key enabler of next-generation intelligent systems operating beyond conventional material and environmental limits.

Author Contributions

H.T. designed this study. H.T., P.M. and Y.Z. collectively conducted the literature review and wrote the manuscript. H.T., Q.Z., W.Z., R.G. and G.Z. provided suggestions and revised the manuscript.

Acknowledgments

This work was financially supported by the National Natural Science Foundation of China (Grant No. 6250030237) and the Shanghai Natural Science Foundation (Grant No. 25ZR1402023), the State Key Laboratory of Widegap Semiconductor Optoelectronic Materials and Technologies (Open Fund Project No. SOMAT-2025-06), and the Shanghai Research Center for Silicon Carbide Power Devices Engineering & Technology Project (Grant No. 19DZ2253400). A chat generative pretrained transformer (ChatGPT, OpenAI) was used for language assistance.

Conflicts of Interest

The authors declare no conflicts of interest.

Data Availability Statement

Data are available upon request from the authors.

References

1. D. Kudithipudi, C. Schuman, C. M. Vineyard, et al., "Neuromorphic Computing at Scale," *Nature* 637, no. 8047 (2025): 801–812, https://doi.org/10.1038/s41586-024-08253-8.

2. H. Tang, N. Yu, P. Min, R. Guo, and G. Zhang, "In-Sensor-Memory Computing for Post-Von Neumann Intelligence: A Perspective," *Nano-Micro Letters* 18, no. 1 (2026): 338, https://doi.org/10.1007/s40820-026-02191-y.

3. V. Jacintha, S. Maheswari, G. Kalpanadevi, A. L. Narayana, and N. Vinodhkumar, "Advancing Gallium Nitride LED Technology: Principles, Challenges, and Future Directions," *Journal of Materials Science* 60, no. 32 (2025): 13781–13834, https://doi.org/10.1007/s10853-025-11216-7.

4. D. Guo, Q. Guo, Z. Chen, Z. Wu, P. Li, and W. Tang, "Review of Ga2O3-Based Optoelectronic Devices," *Materials Today Physics* 11 (2019): 100157, https://doi.org/10.1016/j.mtphys.2019.100157.

5. S. Zhang, Y. Ren, X. Yang, et al., "Crystal Growth Principles, Methods, Properties of Silicon Carbide and Its New Process Prepared From Silicon Cutting Waste," *Journal of Materials Research and Technology* 34 (2025): 2593–2608, https://doi.org/10.1016/j.jmrt.2024.12.239.

6. Z. Xie, K. Jiang, S. Zhang, et al., "Ultraviolet Optoelectronic Synapse Based on AlScN/p-i-n GaN Heterojunction for Advanced Artificial Vision Systems," *Advances in Materials* 37, no. 19 (2025): 2419316, https://doi.org/10.1002/adma.202419316.

7. D. Das, *Carbon-Based Nanofillers Their Rubber Nanocomposites*, (Elsevier, 2019), 123–181.

8. Y. Yang, H. Li, and Q. Hua, "III-Nitride Memristors: Materials, Devices, and Applications," *Materials Futures* 4, no. 3 (2025): 032701, https://doi.org/10.1088/2752-5724/ade5be.

9. C. Kai, Y. Wang, X. Liu, et al., "AlGaN/GaN-Based Optoelectronic Synaptic Devices for Neuromorphic Computing," *Advanced Optical Materials* 11, no. 7 (2023): 2202105, https://doi.org/10.1002/adom.202202105.

10. H. Yang, J. Sun, H. Wang, H. Li, and B. Yang, "A Review of Oriented Wurtzite-Structure Aluminum Nitride Films," *Journal of Alloys and Compounds* 989 (2024): 174330, https://doi.org/10.1016/j.jallcom.2024.174330.

11. N. Izyumskaya, D. O. Demchenko, S. Das, Ü. Özgür, V. Avrutin, and H. Morkoç, "Recent Development of Boron Nitride Towards Electronic Applications," *Advanced Electronic Materials* 3, no. 5 (2017): 1600485, https://doi.org/10.1002/aelm.201600485.

12. A. G. Holmes-Siedle, "Gallium Nitride, a Valuable Semiconductor," *Nature* 252, no. 5483 (1974): 443–444, https://doi.org/10.1038/252443a0.

13. K. Xu and J. Huang, *Growth Appl. AlN Single Cryst* K. Xu and J. Huang, eds. (Springer Nature, 2025), 1–15.

14. A. Kale, R. S. Brusa, and A. Miotello, "Structural and Electrical Properties of AlN Films Deposited Using Reactive RF Magnetron Sputtering for Solar Concentrator Application," *Applied Surface Science* 258, no. 8 (2012): 3450–3454, https://doi.org/10.1016/j.apsusc.2011.11.095.

15. Y. Zhang, Q. Zhu, B. Tian, and C. Duan, "New-Generation Ferroelectric AlScN Materials," *Nano-Micro Letters* 16, no. 1 (2024): 227, https://doi.org/10.1007/s40820-024-01441-1.

16. Z. Liu, Y. Gong, W. Zhou, et al., "Ultrathin High-Temperature Oxidation-Resistant Coatings of Hexagonal Boron Nitride," *Nature Communications* 4, no. 1 (2013): 2541, https://doi.org/10.1038/ncomms3541.

17. H. Jiang and J. Lin, "Hexagonal Boron Nitride: Physical Properties, Hydride Vapor-Phase Epitaxy Growth of Large-Diameter Quasi-Bulk Wafers and Applications," *Physica Status Solidi B: Basic Solid State Physics* 263, no. 1 (2026): e202400605, https://doi.org/10.1002/pssb.202400605.

18. A. C. Khot, T. D. Dongale, K. A. Nirmal, et al., "Amorphous Boron Nitride Memristive Device for High-Density Memory and Neuromorphic Computing Applications," *ACS Applied Materials and Interfaces* 14, no. 8 (2022): 10546–10557, https://doi.org/10.1021/acsami.1c23268.

19. M. Qiu, Z. Jia, M. Yang, et al., "High Detectivity Solar Blind Photodetector Based on Mechanical Exfoliated Hexagonal Boron Nitride

Films," *Nanotechnology* 34, no. 28 (2023): 285204, https://doi.org/10.1088/1361-6528/acccfd.

20. S. Hong, C.-S. Lee, M.-H. Lee, et al., "Ultralow-Dielectric-Constant Amorphous Boron Nitride," *Nature* 582, no. 7813 (2020): 511–514, https://doi.org/10.1038/s41586-020-2375-9.

21. P. E, P. K. B, C. B, E. Manikandan, and L. Agarwal, "A Comprehensive Review of Recent Progress, Prospect and Challenges of Silicon Carbide and Its Applications," *Silicon* 14, no. 18 (2022): 12887–12900, https://doi.org/10.1007/s12633-022-01998-9.

22. D.-Y. Guo, P.-G. Li, Z.-W. Chen, Z.-P. Wu, and W.-H. Tang, and Center for Optoelectronics Materials and Devices, "Beijing University of Posts and Telecommunications, Beijing 100876, China," *Acta Physica Sinica* 68, no. 7 (2019): 078501: Department of Physics, Zhejiang Sci-Tech University, Hangzhou 310018, China, Laboratory of Information Functional Materials and Devices, School of Science, Beijing University of Posts and Telecommunications, Beijing 100876, China, State Key Laboratory of Information Photonics and Optical Communications, https://doi.org/10.7498/aps.68.20181845.

23. S. J. Pearton, J. Yang, P. H. Cary IV, et al., "A Review of Ga2O3 Materials, Processing, and Devices," *Applied Physics Reviews* 5, no. 1 (2018): 011301, https://doi.org/10.1063/1.5006941.

24. R. Khan, N. U. Rehman, R. Thangappan, A. Saritha, and S. Sangaraju, "Advances in Ga_2O_3-Based Memristor Devices, Modeling, Properties, and Applications for Low Power Neuromorphic Computing," *Nanoscale* 17, no. 18 (2025): 11152–11190, https://doi.org/10.1039/d4nr04865b.

25. Y. Lu, C. Lin, and C. Shan, "Optoelectronic Diamond: Growth, Properties, and Photodetection Applications," *Advanced Optical Materials* 6, no. 20 (2018): 1800359, https://doi.org/10.1002/adom.201800359.

26. Z. Liu, B. Yang, P. Liu, et al., "A Diamond-Based Neuromorphic Retina Perception System With Wide Spectrum Photoresponse and Wavelength Sensitivity," *ACS Nano* 19, no. 22 (2025): 21130–21142, https://doi.org/10.1021/acsnano.5c05737.

27. X. Yang, B. Wu, P.-P. Chen, et al., "Diamond Based Optical Metasurfaces for Broadband Wavefront Shaping in Harsh Environment," *Laser & Photonics Reviews* 18, no. 9 (2024): 2400007, https://doi.org/10.1002/lpor.202400007.

28. J. H. Eggert, D. G. Hicks, P. M. Celliers, et al., "Melting Temperature of Diamond at Ultrahigh pressure," *Nature Physics* 6, no. 1 (2010): 40–43, https://doi.org/10.1038/nphys1438.

29. H. Iwane, G. Saito, S. Muto, and K. Ueda, "Diamond/graphene (Carbon Sp3-Sp2) Heterojunctions for Neuromorphic Device Applications," *Journal of Materials Research* 39, no. 15 (2024): 2107–2114, https://doi.org/10.1557/s43578-024-01395-5.

30. P. Thakkar, J. Gosai, H. J. Gogoi, and A. Solanki, "From Fundamentals to Frontiers: A Review of Memristor Mechanisms, Modeling and Emerging Applications," *Journal of Materials Chemistry C* 12, no. 5 (2024): 1583–1608, https://doi.org/10.1039/d3tc03692h.

31. X. Shen, L. Zhang, L. Liu, Y. An, Z. Gao, and P. Guo, "Bipolar Resistive Switching of Pt/Ga_2O_{3-x}/SiC/Pt Thin Film With Ultrahigh OFF/ON Resistance Ratios," *Nanotechnology* 31, no. 22 (2020): 225206, https://doi.org/10.1088/1361-6528/ab758d.

32. L. Chua, "Memristor-The Missing Circuit Element," *IEEE Transactions on Circuit Theory* 18, no. 5 (1971): 507–519, https://doi.org/10.1109/tct.1971.1083337.

33. J. C. Eccles and J. C. Jaeger, "The Relationship Between the Mode of Operation and the Dimensions of the Junctional Regions at Synapses and Motor End-Organs," *Proceedings of the Royal Society of London Series B Biological Sciences* 148, no. 930 (1958): 38–56, https://doi.org/10.1098/rspb.1958.0003.

34. M. V. L. Bennett, "Electrical Synapses, a Personal Perspective (Or History)," *Brain Research Reviews* 32, no. 1 (2000): 16–28, https://doi.org/10.1016/s0165-0173(99)00065-x.

35. P. Alcamí and A. E. Pereda, "Beyond Plasticity: The Dynamic Impact of Electrical Synapses on Neural Circuits," *Nature Reviews Neuroscience* 20, no. 5 (2019): 253–271, https://doi.org/10.1038/s41583-019-0133-5.

36. T. Jiang and D. Ji, "Recent Progress in Flexible Synaptic Transistors: From Materials, Structures to Applications," *Science China Materials* 68, no. 9 (2025): 3019–3041, https://doi.org/10.1007/s40843-025-3405-y.

37. S. L. Palay, "Synapses in the central nervous system," *Journal of Cell Biology* 2, no. 4 (1956): 193–202, https://doi.org/10.1083/jcb.2.4.193.

38. S. R. Sinha, L.-G. Wu, and P. Saggau, "Presynaptic Calcium Dynamics and Transmitter Release Evoked by Single Action Potentials at Mammalian Central Synapses," *Biophysical Journal* 72, no. 2 (1997): 637–651, https://doi.org/10.1016/s0006-3495(97)78702-2.

39. J. Schiller, Y. Schiller, and D. E. Clapham, "NMDA Receptors Amplify Calcium Influx Into Dendritic Spines During Associative Pre- and Postsynaptic Activation," *Nature Neuroscience* 1, no. 2 (1998): 114–118, https://doi.org/10.1038/363.

40. T. Hongo, E. Jankowska, and A. Lundberg, "Post-Synaptic Excitation and Inhibition From Primary Afferents in Neurones of the Spinocervical Tract," *Journal of Physiology* 199, no. 3 (1968): 569–592, https://doi.org/10.1113/jphysiol.1968.sp008669.

41. E. Eide, L. Fedina, J. Jansen, A. Lundberg, and L. Vyklický, "Unitary Excitatory Postsynaptic Potentials in Clarke's Column Neurones," *Nature* 215, no. 5106 (1967): 1176–1177, https://doi.org/10.1038/2151176a0.

42. W. S. McCulloch and W. Pitts, "A Logical Calculus of the Ideas Immanent in Nervous Activity," *Bulletin of Mathematical Biophysics* 5, no. 4 (1943): 115–133, https://doi.org/10.1007/bf02478259.

43. B. E. Alger and T. J. Teyler, "Long-Term and Short-Term Plasticity in the CA1, CA3, and Dentate Regions of the Rat Hippocampal Slice," *Brain Research* 110, no. 3 (1976): 463–480, https://doi.org/10.1016/0006-8993(76)90858-1.

44. V. F. Castellucci, T. J. Carew, and E. R. Kandel, "Cellular Analysis of Long-Term Habituation of the Gill-Withdrawal Reflex of *Aplysia Californica*," *Science* 202, no. 4374 (1978): 1306–1308, https://doi.org/10.1126/science.214854.

45. B. Katz and R. Miledi, "The Role of Calcium in Neuromuscular Facilitation," *Journal of Physiology* 195, no. 2 (1968): 481–492, https://doi.org/10.1113/jphysiol.1968.sp008469.

46. W. F. White, J. V. Nadler, and C. W. Cotman, "Analysis of Short-Term Plasticity at the Perforant Path-Granule Cell Synapse," *Brain Research* 178, no. 1 (1979): 41–53, https://doi.org/10.1016/0006-8993(79)90086-6.

47. D. O. Hebb, *The Organization of Behavior* (Psychology Press, 2005).

48. Z. Xia, X. Sun, Z. Wang, J. Meng, B. Jin, and T. Wang, "Low-Power Memristor for Neuromorphic Computing: From Materials to Applications," *Nano-Micro Letters* 17, no. 1 (2025): 217, https://doi.org/10.1007/s40820-025-01705-4.

49. W. Xu, S.-Y. Min, H. Hwang, and T.-W. Lee, "Organic Core-Sheath Nanowire Artificial Synapses With Femtojoule Energy Consumption," *Science Advances* 2, no. 6 (2016): e1501326, https://doi.org/10.1126/sciadv.1501326.

50. D. B. Strukov, G. S. Snider, D. R. Stewart, and R. S. Williams, "The Missing Memristor Found," *Nature* 453, no. 7191 (2008): 80–83, https://doi.org/10.1038/nature06932.

51. F. Pan, C. Chen, Z. Wang, Y. Yang, J. Yang, and F. Zeng, "Nonvolatile Resistive Switching Memories-Characteristics, Mechanisms and

Challenges," *Progress in Natural Science: Materials International* 20 (2010): 1–15, https://doi.org/10.1016/s1002-0071(12)60001-x.

52. R. Muenstermann, T. Menke, R. Dittmann, and R. Waser, "Coexistence of Filamentary and Homogeneous Resistive Switching in Fe-Doped $SrTiO_3$ Thin-Film Memristive Devices," *Advances in Materials* 22, no. 43 (2010): 4819–4822, https://doi.org/10.1002/adma.201001872.

53. W. Xia, X. Sun, Y. Yin, C. Jia, G. Li, and W. Zhang, "Origin of Resistance State Relaxation and Nonvolatile Features in NiO Films: Interfacial vs Filamentary Resistive Switching," *AIP Advances* 10 (2020): 105319, https://doi.org/10.1063/5.0007173.

54. H. Liu, Q. Hua, R. Yu, et al., "A Bamboo-Like GaN Microwire-Based Piezotronic Memristor," *Advances in Functional Materials* 26, no. 29 (2016): 5307–5314, https://doi.org/10.1002/adfm.201600962.

55. Q. Hua, J. Sun, H. Liu, et al., "Flexible GaN Microwire-Based Piezotronic Sensory Memory Device," *Nano Energy* 78 (2020): 105312, https://doi.org/10.1016/j.nanoen.2020.105312.

56. Y. Ji, A. Huang, M. Yang, et al., "Wrinkled-Surface-Induced Memristive Behavior of MoS_2 Wrapped GaN Nanowires," *Advanced Electronic Materials* 6, no. 10 (2020): 2000571, https://doi.org/10.1002/aelm.202000571.

57. C. Huang, C. Wu, Y. Lin, Y. Chou, and K. Lee, "Wet-Etching-Boosted Charge Storage in 1D Nitride-Based Systems for Imitating Biological Synaptic Behaviors," *Advances in Functional Materials* 33, no. 52 (2023): 2306030, https://doi.org/10.1002/adfm.202306030.

58. Q. Hua, X. Cui, H. Liu, C. Pan, W. Hu, and Z. L. Wang, "Piezotronic Synapse Based on a Single GaN Microwire for Artificial Sensory Systems," *Nano Letters* 20, no. 5 (2020): 3761–3768, https://doi.org/10.1021/acs.nanolett.0c00733.

59. Z. Zhang, B. Gao, Z. Fang, et al., "All-Metal-Nitride RRAM Devices," *IEEE Electron Device Letters* 36, no. 1 (2015): 29–31, https://doi.org/10.1109/led.2014.2367542.

60. B. J. Choi, A. C. Torrezan, J. P. Strachan, et al., "High-Speed and Low-Energy Nitride Memristors," *Advances in Functional Materials* 26, no. 29 (2016): 5290–5296, https://doi.org/10.1002/adfm.201600680.

61. Y. Guo, W. Hu, C. Zhang, Y. Peng, and Y. Guo, "An Electronic Synapse Device Based on Aluminum Nitride Memristor for Neuromorphic Computing Application," *Journal of Physics D: Applied Physics* 53, no. 19 (2020): 195101, https://doi.org/10.1088/1361-6463/ab7517.

62. O. Kwon, Y. Lee, M. Kang, and S. Kim, "Synaptic Plasticity Features and Neuromorphic System Simulation in AlN-Based Memristor Devices," *Journal of Alloys and Compounds* 911 (2022): 164870, https://doi.org/10.1016/j.jallcom.2022.164870.

63. Y. Zhang, G. Tang, P. Feng, et al., "Neutron Radiation-Resistant Aluminum Nitride Memristor," *Applied Physics Letters* 121, no. 16 (2022): 163502, https://doi.org/10.1063/5.0107956.

64. C.-H. Ling, T.-W. Yu, C.-H. Chuang, C.-L. Mo, J.-J. Shyue, and M.-J. Chen, "Atomic Layer Annealing for Spatial Tailoring in Sub-4 nm AlN RRAM Devices With Low-Voltage Operation," *Journal of Alloys and Compounds* 991 (2024): 174535, https://doi.org/10.1016/j.jallcom.2024.174535.

65. S. K. Mohanty, D. Panda, C.-H. Wu, and K.-M. Chang, "Controlling Diffusion Dynamics With Electrode Engineering for Stable and Reliable Resistive Switching in AlN/Ag-Based CBRAM," *Materials Today Proceedings* (2023), https://doi.org/10.1016/j.matpr.2023.05.497.

66. H. Guo, J. Yao, S. Chen, et al., "Enhancing Resistive Switching in AlN-Based Memristors through Oxidative Al2O3 Layer Formation: A Study on Preparation Techniques and Performance Impact," *Micromachines* 15, no. 12 (2024): 1499, https://doi.org/10.3390/mi15121499.

67. J. Choi, H. Park, Y. Byun, Y. Seo, and S. Kim, "Polarity-Dependent Dual-Mode AlN-Embedded RRAM With Improved Stochastic Switching and Synaptic Modulation for Neuromorphic Computing," *Journal of Chemical Physics* 163, no. 16 (2025): 164707, https://doi.org/10.1063/5.0298600.

68. J. Kim, S. Lee, Y. Seo, and S. Kim, "Emulating Biological Synaptic Characteristics of HfOx/AlN-Based 3D Vertical Resistive Memory for Neuromorphic Systems," *Journal of Chemical Physics* 160, no. 14 (2024): 144703, https://doi.org/10.1063/5.0202610.

69. J. Park, H. Jang, Y. Byun, H. Na, H. Ji, and S. Kim, "Improved Memory and Synaptic Device Performance of HfO2-Based Multilayer Memristor by Inserting Oxygen Gradient TiOx Layer," *Chaos, Solitons & Fractals* 191 (2025): 115910, https://doi.org/10.1016/j.chaos.2024.115910.

70. X. Dai, Q. Hua, C. Jiang, et al., "Artificial Synapse Based on a Tri-Layer AlN/AlScN/AlN Stacked Memristor for Neuromorphic Computing," *Nano Energy* 124 (2024): 109473, https://doi.org/10.1016/j.nanoen.2024.109473.

71. D. Wang, P. Wang, S. Mondal, et al., "Ultrathin Nitride Ferroic Memory With Large ON/OFF Ratios for Analog In-Memory Computing," *Advances in Materials* 35, no. 20 (2023): 2210628, https://doi.org/10.1002/adma.202210628.

72. C. Han, H. Qin, R. Hu, et al., "Non-Volatile, High on/off Ratio, Durable Memristor Devices Based on ScAlN for Artificial Synapse," *Materials Science in Semiconductor Processing* 201 (2026): 110025, https://doi.org/10.1016/j.mssp.2025.110025.

73. S. S. Teja Nibhanupudi, A. Roy, D. Veksler, et al., "Ultra-Fast Switching Memristors Based on Two-Dimensional Materials," *Nature Communications* 15, no. 1 (2024): 2334, https://doi.org/10.1038/s41467-024-46372-y.

74. J. Xie, M. N. Patoary, M. A. Rahman Laskar, et al., "Quantum Conductance in Vertical Hexagonal Boron Nitride Memristors With Graphene-Edge Contacts," *Nano Letters* 24, no. 8 (2024): 2473–2480, https://doi.org/10.1021/acs.nanolett.3c04057.

75. L. Völkel, D. Braun, M. Belete, et al., "Resistive Switching and Current Conduction Mechanisms in Hexagonal Boron Nitride Threshold Memristors With Nickel Electrodes," *Advances in Functional Materials* 34, no. 15 (2024): 2300428, https://doi.org/10.1002/adfm.202300428.

76. J. Ge, H. Huang, Z. Ma, et al., "A Sub-500 mV Monolayer Hexagonal Boron Nitride Based Memory Device," *Materials and Design* 198 (2021): 109366, https://doi.org/10.1016/j.matdes.2020.109366.

77. C. Chen, S. Gao, G. Tang, et al., "Effect of Electrode Materials on AlN-Based Bipolar and Complementary Resistive Switching," *ACS Applied Materials and Interfaces* 5 (2013): 1793–1799, https://doi.org/10.1021/am303128h.

78. S. Suman, N. Mukurala, L. Mohapatra, and A. K. Kushwaha, "Single Step Wet-Chemical Deposition of Cesium Doped β-Ga2O3 Nanostructured Films for Memristor Application," *Memories-Materials, Devices, Circuits and Systems* 2 (2022): 100015, https://doi.org/10.1016/j.memori.2022.100015.

79. S. Zhang, Y. Tao, S. Qin, et al., "Memristors Based on Two-Dimensional H-BN Materials: Synthesis, Mechanism, Optimization and Application," *npj 2D Materials and Applications* 8, no. 1 (2024): 81, https://doi.org/10.1038/s41699-024-00519-z.

80. Y. Deng, Y. Li, P. Wang, S. Wang, X. Pan, and D. Wang, "Observation of Resistive Switching in a Graphite/Hexagonal Boron Nitride/Graphite Heterostructure Memristor," *Journal of Semiconductors* 43, no. 5 (2022): 052003, https://doi.org/10.1088/1674-4926/43/5/052003.

81. C. Pan, Y. Ji, N. Xiao, et al., "Coexistence of Grain-Boundaries-Assisted Bipolar and Threshold Resistive Switching in Multilayer Hexagonal Boron Nitride," *Advances in Functional Materials* 27, no. 10 (2017): 1604811, https://doi.org/10.1002/adfm.201604811.

82. K. Zhu, X. Liang, B. Yuan, et al., "Graphene–Boron Nitride–-Graphene Cross-Point Memristors With Three Stable Resistive States," *ACS Applied Materials and Interfaces* 11, no. 41 (2019): 37999–38005, https://doi.org/10.1021/acsami.9b04412.

83. H. Suzuki, M. Kishibuchi, K. Shimogami, et al., "Memristive Behavior in One-Dimensional Hexagonal Boron Nitride/Carbon Nanotube Heterostructure Assemblies," *ACS Applied Electronic Materials* 3, no. 8 (2021): 3555–3566, https://doi.org/10.1021/acsaelm.1c00472.

84. W. Lee, M. Siddik, S. Jung, et al., "Effect of $Ge_2Sb_2Te_5$ Thermal Barrier on Reset Operations in Filament-type Resistive Memory," *IEEE Electron Device Letters* 32, no. 11 (2011): 1573–1575, https://doi.org/10.1109/led.2011.2163614.

85. L. Zhong, P. A. Reed, R. Huang, C. H. de Groot, and L. Jiang, "Resistive Switching of Cu/SiC/Au Memory Devices With a High ON/OFF Ratio," *Solid State Electronics* 94 (2014): 98–102, https://doi.org/10.1016/j.sse.2014.02.013.

86. L. Chen, Z. Ma, K. Leng, et al., "Artificial Synapse Consisted of TiSbTe/SiCx: H Memristor With Ultra-High Uniformity for Neuromorphic Computing," *Nanomaterials* 12 (2022): 2110, https://doi.org/10.3390/nano12122110.

87. L. Liu, J. Zhao, G. Cao, S. Zheng, and X. Yan, "A Memristor-Based Silicon Carbide for Artificial Nociceptor and Neuromorphic Computing," *Advanced Materials Technologies* 6, no. 12 (2021): 2100373, https://doi.org/10.1002/admt.202100373.

88. H. Qin, S. Sun, N. He, et al., "Wide-Bandgap Semiconductor SiC-Based Memristors Fabricated Entirely by Electron Beam Evaporation for Artificial Synapses," *Applied Physics Letters* 125, no. 14 (2024): 143502, https://doi.org/10.1063/5.0230471.

89. O. Kapur, D. Guo, J. Reynolds, et al., "Back-End-of-Line SiC-Based Memristor for Resistive Memory and Artificial Synapse," *Advanced Electronic Materials* 8, no. 9 (2022): 2200312, https://doi.org/10.1002/aelm.202200312.

90. O. Kapur, D. Guo, J. Reynolds, et al., "An Ultra High-Endurance Memristor Using Back-End-of-Line Amorphous SiC," *Scientific Reports* 14, no. 1 (2024): 14008, https://doi.org/10.1038/s41598-024-64499-2.

91. B. Santra, M.-A. Luong, B. Mondal, A. Claverie, and A. Kanjilal, "Forming-Free Multilevel Resistive Switching in a ZnO@β-SiC Composite for Neuromorphic Computing," *ACS Applied Electronic Materials* 6, no. 11 (2024): 8008–8019, https://doi.org/10.1021/acsaelm.4c01331.

92. B. Santra, G. Das, G. Aquilanti, and A. Kanjilal, "Resistive Switching and Synaptic Characteristics in ZnO@β-SiC Composite-Based RRAM for Neuromorphic Computing," *Journal of Applied Physics* 137, no. 4 (2025): 044501, https://doi.org/10.1063/5.0246384.

93. H. Qin, S. Sun, N. He, Y. Liu, X. Wang, and Y. Tong, *2024 IEEE Int. Conf. IC Des. Technol. ICICDT*, (2024), 1–3.

94. Z. Zuo, C. Zhou, Z. Ma, et al., "Flexible Artificial Ag NPs: A–SiC0.11: H Synapse on Al Foil With High Uniformity and On/Off Ratio for Neuromorphic Computing," *Nanomaterials* 14, no. 18 (2024): 1474, https://doi.org/10.3390/nano14181474.

95. W. Li, J. Wan, Z. Tu, H. Li, H. Wu, and C. Liu, "Optimizing Endurance Performance of Ga2O3 Random Resistive Access Memories by Altering Oxygen Vacancy Content," *Ceramics International* 48, no. 3 (2022): 3185–3191, https://doi.org/10.1016/j.ceramint.2021.10.091.

96. W.-L. Huang, Y.-Z. Lin, S.-P. Chang, W.-C. Lai, and S.-J. Chang, "Stability-Enhanced Resistive Random-Access Memory via Stacked $In_xGa_{1-x}O$ by the RF Sputtering Method," *ACS Omega* 6, no. 16 (2021): 10691–10697, https://doi.org/10.1021/acsomega.1c00112.

97. H. J. Lee, J.-H. Kim, H.-J. Kim, and S.-N. Lee, "Improvements in Resistive and Capacitive Switching Behaviors in Ga2O3 Memristors via High-Temperature Annealing Process," *Materials* 17, no. 11 (2024): 2727, https://doi.org/10.3390/ma17112727.

98. H. Nan, B. Guokai, C. Kunfang, et al., "Lattice-Engineered High-Quality β-Ga2O3 Membranes for Memristive Applications Towards Image Encryption, Decryption, and Edge Detection," *Science China Materials* (2025), https://doi.org/10.1007/s40843-025-3858-8.

99. X. Dai, X. Zhang, D. Gong, and G. Xiang, "Performance Enhancement and In Situ Observation of Resistive Switching and Magnetic Modulation by a Tunable Two-Level System of Mn Dopants in *a*-Gallium Oxide-Based Memristor," *Advances in Functional Materials* 33, no. 49 (2023): 2304749, https://doi.org/10.1002/adfm.202304749.

100. C. Sivakumar, G.-H. Tsai, P.-F. Chung, B. Balraj, Y.-F. Lin, and M.-S. Ho, "High-Quality Single-Crystalline β-Ga2O3 Nanowires: Synthesis to Nonvolatile Memory Applications," *Nanomaterials* 11, no. 8 (2021): 2013, https://doi.org/10.3390/nano11082013.

101. Y. Aoki, C. Wiemann, V. Feyer, et al., "Bulk Mixed Ion Electron Conduction in Amorphous Gallium Oxide Causes Memristive Behaviour," *Nature Communications* 5, no. 1 (2014): 3473, https://doi.org/10.1038/ncomms4473.

102. L.-W. Wang, C.-W. Huang, K.-J. Lee, S.-Y. Chu, and Y.-H. Wang, "Multi-Level Resistive Al/Ga2O3/ITO Switching Devices With Interlayers of Graphene Oxide for Neuromorphic Computing," *Nanomaterials* 13, no. 12 (2023): 1851, https://doi.org/10.3390/nano13121851.

103. W. Li-Wen, H. Chih-Wei, L. Ke-Jing, and C. Sheng-Yuan, W. Yeong-Her, Switching Performance Enhancement in Gallium Oxide-Based Multilevel RRAM Devices Using Graphene Oxide Insertion Layer (2023), https://doi.org/10.20944/preprints202305.0592.v1.

104. K.-J. Gan, P.-T. Liu, T.-C. Chien, D.-B. Ruan, and S. M. Sze, "Highly Durable and Flexible Gallium-Based Oxide Conductive-Bridging Random Access Memory," *Scientific Reports* 9, no. 1 (2019): 14141, https://doi.org/10.1038/s41598-019-50816-7.

105. M. N. Almadhoun, M. Speckbacher, B. C. Olsen, et al., "Bipolar Resistive Switching in Junctions of Gallium Oxide and P-Type Silicon," *Nano Letters* 21, no. 6 (2021): 2666–2674, https://doi.org/10.1021/acs.nanolett.1c00539.

106. X. Li, J.-G. Yang, H.-P. Ma, et al., "Atomic Layer Deposition of Ga_2O_3/ZnO Composite Films for High-Performance Forming-Free Resistive Switching Memory," *ACS Applied Materials and Interfaces* 12, no. 27 (2020): 30538–30547, https://doi.org/10.1021/acsami.0c06476.

107. K.-J. Gan, P.-T. Liu, Y.-C. Chiu, D.-B. Ruan, T.-C. Chien, and S. M. Sze, "TAOS Based Cu/TiW/IGZO/Ga2O3/Pt Bilayer CBRAM for Low-Power Display Technology," *Surface Coatings Technology* 354 (2018): 169–174, https://doi.org/10.1016/j.surfcoat.2018.08.093.

108. S. Battistoni, R. Carcione, E. Tamburri, V. Erokhin, M. L. Terranova, and S. Iannotta, "A Ti-Doped Chemical Vapor Deposition Diamond Device as Artificial Synapse for Neuromorphic Applications," *Advanced Materials Technologies* 8, no. 9 (2023): 2201555, https://doi.org/10.1002/admt.202201555.

109. P. Liu, T. Shao, Q. Chen, and A. H. Shen, "Ultralow Threshold Voltage Responding Synaptic Memristor Device Based on Cu_xO and Diamond Schottky Junction," *Physica Status Solidi A: Applications and Materials Science* 222, no. 6 (2025): 2400707, https://doi.org/10.1002/pssa.202400707.

110. X. Hua, J. Zheng, X. Han, et al., "Artificial Optoelectronic Synapse With Nanolayered GaN/AlN Periodic Structure for Neuromorphic Computing," *ACS Applied Nano Materials* 6, no. 10 (2023): 8461–8467, https://doi.org/10.1021/acsanm.3c00796.

111. Z. Xie, K. Jiang, S. Zhang, et al., "Nonvolatile and Reconfigurable Two-Terminal Electro-Optic Duplex Memristor Based on III-Nitride Semiconductors," *Light: Science & Applications* 13, no. 1 (2024): 78, https://doi.org/10.1038/s41377-024-01422-4.

112. Y.-H. Ji, Q. Gao, A.-P. Huang, et al., "GaO_x@GaN Nanowire Arrays on Flexible Graphite Paper With Tunable Persistent Photoconductivity,"

ACS Applied Materials and Interfaces 13, no. 35 (2021): 41916–41925, https://doi.org/10.1021/acsami.1c13355.

113. M. Chen, G. Wei, S. Yuan, et al., "Low-Power Plasmonic SiC Nanowire Network-Based Artificial Photo-Synaptic Device for Musical Classification Neural Network Systems," *Science China Materials* 68, no. 10 (2025): 3703–3714, https://doi.org/10.1007/s40843-025-3489-5.

114. X. Liu, D. Wang, W. Chen, et al., "Optoelectronic Synapses With Chemical-Electric Behaviors in Gallium Nitride Semiconductors for Biorealistic Neuromorphic Functionality," *Nature Communications* 15, no. 1 (2024): 7671, https://doi.org/10.1038/s41467-024-51194-z.

115. Z. Gao, X. Ju, H. Yu, et al., "Ultrathin Gallium Nitride Quantum-Disk-in-Nanowire-Enabled Reconfigurable Bioinspired Sensor for High-Accuracy Human Action Recognition," *Nano-Micro Letters* 18, no. 1 (2026): 54, https://doi.org/10.1007/s40820-025-01888-w.

116. G. Zhang, W. Liu, N. Huo, et al., "Vertical Monolithic SiC Optoelectronic Synapses With Visible-Light Neuromorphic Plasticity," *ACS Applied Electronic Materials* 7, no. 14 (2025): 6560–6569, https://doi.org/10.1021/acsaelm.5c00873.

117. S. Feng, J. Li, L. Feng, et al., "Dual-Mode Conversion of Photodetector and Neuromorphic Vision Sensor via Bias Voltage Regulation on a Single Device," *Advances in Materials* 35, no. 49 (2023): 2308090, https://doi.org/10.1002/adma.202308090.

118. Y. Mizuno, Y. Ito, and K. Ueda, "Optoelectronic Synapses Using Vertically Aligned Graphene/Diamond Heterojunctions," *Carbon* 182 (2021): 669–676, https://doi.org/10.1016/j.carbon.2021.06.060.

119. X. Miao, Y. Zhang, Y. Lin, H. Lei, T. Min, and Y. Pan, "Robust Self-Powered Optoelectronic Synapses Based on Epitaxial InSe/GaN Heterojunction With Interfacial Charge-Trapping Layer," *Advanced Optical Materials* 12, no. 19 (2024): 2400358, https://doi.org/10.1002/adom.202400358.

120. D. Y. Guo, X. L. Zhao, Y. S. Zhi, et al., "Epitaxial Growth and Solar-Blind Photoelectric Properties of Corundum-Structured α -Ga 2 O 3 Thin Films," *Materials Letters* 164 (2016): 364–367, https://doi.org/10.1016/j.matlet.2015.11.001.

121. J. Kim, H. J. Lee, H. Kim, et al., "Oxide Semiconductor Memristor-Based Optoelectronic Synaptic Devices With Quaternary Memory Storage," *Advanced Electronic Materials* 10, no. 7 (2024): 2300863, https://doi.org/10.1002/aelm.202300863.

122. H. Fan, H. Wang, W. Chen, et al., "Zn-doped Ga2O3 Based Two-Terminal Artificial Synapses for Neuromorphic Computing Applications," *Science China Materials* 68, no. 10 (2025): 3767–3777, https://doi.org/10.1007/s40843-025-3498-5.

123. Y. Liang, F. Zhang, S. Qi, et al., "Deep Ultraviolet Optoelectronic Memristors Based on Gallium Oxide for Biomimetic Visual Processing and Neuromorphic Memory Applications," *Applied Physics Letters* 126, no. 14 (2025): 141102, https://doi.org/10.1063/5.0259184.

124. L. Yang, X. Gu, M. Zhou, J. Zhang, Y. Huang, and Y. Zhao, "Deep-UV-Photo-Excited Synaptic Ga_2O_3 Nano-Device With Low-Energy Consumption for Neuromorphic Computing," *Journal of Semiconductors* 46, no. 2 (2025): 022401, https://doi.org/10.1088/1674-4926/24050037.

125. B. Zhao, C. Wu, H. Wu, F. Wu, S. Wang, and D. Guo, "β-Ga $_2$ O $_3$ Microwire Solar-Blind Photodetectors With High Polarization Ratio for Multifunctional Information Encryption," *Advanced Optical Materials* 13, no. 33 (2025): e02580, https://doi.org/10.1002/adom.202502580.

126. Y. Yao, A. Ahnood, A. Chambers, W. Tong, and S. Prawer, "Nitrogen-Doped Ultrananocrystalline Diamond—Optoelectronic Bio-interface for Wireless Neuronal Stimulation," *Advanced Healthcare Materials* 14, no. 9 (2025): 2403901, https://doi.org/10.1002/adhm.202403901.

127. Y. Lin, L. Zhong, L. Wang, et al., "ITZO/Ga2O3 Heterostructure Memristor With Integrated Optoelectronic Synaptic Function for Neuromorphic Vision Applications," *Chemical Engineering Journal* 525 (2025): 169684, https://doi.org/10.1016/j.cej.2025.169684.

128. R. Li, W. Wang, Y. Li, S. Gao, W. Yue, and G. Shen, "Multi-Modulated Optoelectronic Memristor Based on Ga2O3/MoS2 Heterojunction for Bionic Synapses and Artificial Visual System," *Nano Energy* 111 (2023): 108398, https://doi.org/10.1016/j.nanoen.2023.108398.

129. D. Cui, M. Pei, Z. Lin, et al., "Versatile Optoelectronic Memristor Based on Wide-Bandgap Ga2O3 for Artificial Synapses and Neuromorphic Computing," *Light: Science & Applications* 14, no. 1 (2025): 161, https://doi.org/10.1038/s41377-025-01773-6.

130. M. Lee, S. Nam, B. Cho, et al., "Accelerated Learning in Wide-Band-Gap AlN Artificial Photonic Synaptic Devices: Impact on Suppressed Shallow Trap Level," *Nano Letters* 21, no. 18 (2021): 7879–7886, https://doi.org/10.1021/acs.nanolett.1c01885.

131. M. Zhou, Y. Zhao, X. Gu, et al., "Light-Stimulated Low-Power Artificial Synapse Based on a Single GaN Nanowire for Neuromorphic Computing," *Photonics Research* 11, no. 10 (2023): 1667, https://doi.org/10.1364/prj.487936.

132. Y. Luo, H. Yu, D. Wang, et al., "A Single Diode With Integrated Photosensing, Memory and Processing for Neuromorphic Image Sensors," *Nature Electronics* 9, no. 4 (2026): 404–413, https://doi.org/10.1038/s41928-026-01588-2.

133. X. Sun, D. Wang, X. Wu, et al., "Facile Formation of van der Waals Metal Contact With III-Nitride Semiconductors," *Scientific Bulletin* 69, no. 23 (2024): 3692–3699, https://doi.org/10.1016/j.scib.2024.09.028.

134. H. Wang, P. Li, L. Yang, Z. Jin, J. Ma, and Y. Liu, "Ga_2O_3-Based Optoelectronic Synapse With Piezo/Photo-Gated Modulation for Multimodal Perception," *IEEE Electron Device Letters* 46, no. 9 (2025): 1525–1528, https://doi.org/10.1109/led.2025.3590716.

135. X. Wang, X. She, Y. Wang, Y. Guo, and Y. Liu, *2025 IEEE Int. Conf. Electron Devices Solid-State Circuits EDSS*, (2025), 62–63.

136. Z. Tang, J.-L. Fang, Y.-X. Wu, et al., "Low-Temperature Solution-Processed Amorphous-Ga2O3 Optoelectric Synapses for Neuromorphic Computing," *Optics Laser Technology* 187 (2025): 112837, https://doi.org/10.1016/j.optlastec.2025.112837.

137. J. Wang, Y. Zhang, D. Xie, et al., "Piezo-Phototronic Effect Modulated Optoelectronic Artificial Synapse Based on a-Ga2O3/ZnO Heterojunction," *Nano Energy* 120 (2024): 109128, https://doi.org/10.1016/j.nanoen.2023.109128.

138. P. Li, X. Shan, Y. Lin, et al., "Ultra-Highly Linear Ga2O3-Based Cascade Heterojunctions Optoelectronic Synapse With Thousands of Conductance States for Neuromorphic Visual System," *Light: Science & Applications* 14, no. 1 (2025): 354, https://doi.org/10.1038/s41377-025-01897-9.

139. X. Wang, Y. Wang, H. Peng, et al., "Ultra-Low Power in-Sensor Computing β-Ga_2O_3 Ultraviolet Optoelectronic Synaptic Devices," *IEEE Photonics Technology Letter* 36, no. 23 (2024): 1393–1396, https://doi.org/10.1109/lpt.2024.3483815.

140. X. Liu, Z. Shi, M. Bu, X. Wang, W. Yan, and X. Pi, "4H-SiC Homojunction Photogated Synapses Enabling High-Temperature Neuromorphic Computing," *Small* 21, no. 34 (2025): 2504084, https://doi.org/10.1002/smll.202504084.

141. H. J. Lee, J.-H. Kim, S. H. Lee, and S.-N. Lee, "Ga2O3-Based Optoelectronic Memristor and Memcapacitor Synapse for In-Memory Sensing and Computing Applications," *Nanomaterials* 14, no. 23 (2024): 1972, https://doi.org/10.3390/nano14231972.

142. J. Du, B. Sun, C. Yang, et al., "Ferroelectric Memristor and its Neuromorphic Computing Applications," *Materials Today Physics* 50 (2025): 101607, https://doi.org/10.1016/j.mtphys.2024.101607.

143. D. K. Pradhan, D. C. Moore, G. Kim, et al., "A Scalable Ferroelectric Non-Volatile Memory Operating at 600 °C," *Nature Electronics* 7, no. 5 (2024): 348–355, https://doi.org/10.1038/s41928-024-01148-6.

144. D. Wang, P. Wang, S. Mondal, et al., "An Epitaxial Ferroelectric ScAlN/GaN Heterostructure Memory," *Advanced Electronic Materials* 8, no. 9 (2022): 2200005, https://doi.org/10.1002/aelm.202200005.

145. J. Y. Yang, M. Park, M. J. Yeom, et al., "Reconfigurable Physical Reservoir in GaN/α-In_2Se_3 HEMTs Enabled by Out-of-Plane Local Polarization of Ferroelectric 2D Layer," *ACS Nano* 17, no. 8 (2023): 7695–7704, https://doi.org/10.1021/acsnano.3c00187.

146. M. Park, J. Y. Yang, M. J. Yeom, et al., "An Artificial Neuromuscular Junction for Enhanced Reflexes and Oculomotor Dynamics Based on a Ferroelectric $CuInP_2S_6$/GaN HEMT," *Science Advances* 9, no. 38 (2023): eadh9889, https://doi.org/10.1126/sciadv.adh9889.

147. Q. Liu, B. Gao, P. Yao, et al., *2020 IEEE Int. Solid-State Circuits Conf* (ISSCC, 2020), 500–502.

148. W. Ding, J. Zhu, Z. Wang, et al., "Prediction of Intrinsic Two-Dimensional Ferroelectrics in In2Se3 and Other III2–VI3 van der Waals materials," *Nature Communications* 8, no. 1 (2017): 14956, https://doi.org/10.1038/ncomms14956.

149. C. Diorio, P. Hasler, A. Minch, and C. A. Mead, "A Single-Transistor Silicon Synapse," *IEEE Transactions on Electron Devices* 43, no. 11 (1996): 1972–1980, https://doi.org/10.1109/16.543035.

150. L. Li, H. Liu, Q. Peng, et al., "Neuromorphic Engineering in GaN HEMTs Exploiting Dendritic Dislocations for Neuromodulation Behaviors and Adaptive Intelligent Power Forecasting Systems," *Nano Energy* 130 (2024): 110129, https://doi.org/10.1016/j.nanoen.2024.110129.

151. D. Li, M. Chen, Z. Sun, et al., "Two-Dimensional Non-Volatile Programmable P–N Junctions," *Nature Nanotechnology* 12, no. 9 (2017): 901–906, https://doi.org/10.1038/nnano.2017.104.

152. J. Kim, A. Kumar, J. Kim, et al., "High Power Operating Neuromorphic Transistor Based on F-Doped β-Ga2O3 Channel on Si Wafers," *Journal of Alloys and Compounds* 1039 (2025): 183267, https://doi.org/10.1016/j.jallcom.2025.183267.

153. J. Lin, S. Lan, L. Yang, Q. Lin, Y. Chen, and W. Xu, "Na-doped Ga_2O_3 Electrolyte-Gated Synaptic Transistors for Neuromorphic Computing," *Journal of Materials Chemistry C* 13, no. 26 (2025): 13246–13254, https://doi.org/10.1039/d5tc01248a.

154. Y. Li, H. Song, and J. Jiang, "Vertical Ion-Coupling Ga_2O_3 TFT With Spatiotemporal Logic Encryption," *IEEE Transactions on Electron Devices* 70, no. 6 (2023): 3122–3125, https://doi.org/10.1109/ted.2023.3268145.

155. J. Chen, H. Du, H. Qu, et al., "AlGaN/GaN MOS-HEMT Enabled Optoelectronic Artificial Synaptic Devices for Neuromorphic Computing," *APL Machine Learning* 2 (2024): 026113, https://doi.org/10.1063/5.0194083.

156. J. Yan, Z. Sun, L. Fang, et al., "Light-Stimulated Artificial Synapses With Accelerating Photopic Adaption Based on III-Nitride Heterojunction Transistor," *ACS Photonics* (2024): 4c01038: acsphotonics, https://doi.org/10.1021/acsphotonics.4c01038.

157. K.-C. Chang, H. Liu, X. Duan, Z. Peng, X. Lin, and L. Li, "Optoelectronic Dual-Synapse Based on Wafer-Level GaN-on-Si Device Incorporating Embedded SiO2 Barrier Layers," *Nano Energy* 125 (2024): 109564, https://doi.org/10.1016/j.nanoen.2024.109564.

158. Z. Su, Y. Yan, M. Sun, et al., "Broadband Artificial Tetrachromatic Synaptic Devices Composed of 2D/3D Integrated WSe_2-GaN-Based Dual-Channel Floating Gate Transistors," *Advances in Functional Materials* 34, no. 33 (2024): 2316802, https://doi.org/10.1002/adfm.202316802.

159. X. Hong, Y. Huang, Q. Tian, et al., "Two-Dimensional Perovskite-Gated AlGaN/GaN High-Electron-Mobility-Transistor for Neuromorphic Vision Sensor," *Advanced Science* 9, no. 27 (2022): 2202019, https://doi.org/10.1002/advs.202202019.

160. H. Zhang, F. Liang, L. Yang, et al., "Superior AlGaN/GaN-Based Phototransistors and Arrays With Reconfigurable Triple-Mode Functionalities Enabled by Voltage-Programmed Two-Dimensional Electron Gas for High-Quality Imaging," *Advances in Materials* 36 (2024): 2405874, https://doi.org/10.1002/adma.202405874.

161. Z. Sun, F. Shi, Z. Shi, et al., "GaN Optoelectronic Integrated Chip With Multifunctions of Communication and Neuromorphic Computing," *Advanced Optical Materials* 13, no. 18 (2025): 2403514, https://doi.org/10.1002/adom.202403514.

162. Y. Zhang, W. Liu, K. Liu, et al., "Optoelectronic Neuromorphic Logic Memory Device Based on Ga_2O_3/MoS_2 van der Waals Heterostructure With High Rectification and On/Off Ratios," *Advances in Functional Materials* 34, no. 49 (2024): 2408978, https://doi.org/10.1002/adfm.202408978.

163. X. Liu, W. Huang, C. Kai, et al., "Photogated Synaptic Transistors Based on the Heterostructure of 4H-SiC and Organic Semiconductors for Neuromorphic Ultraviolet Vision," *ACS Applied Electronic Materials* 5, no. 1 (2023): 367–374, https://doi.org/10.1021/acsaelm.2c01390.

164. P. Stoliar, J. Tranchant, B. Corraze, et al., "A Leaky-Integrate-and-Fire Neuron Analog Realized With a Mott Insulator," *Advances in Functional Materials* 27, no. 11 (2017): 1604740, https://doi.org/10.1002/adfm.201604740.

165. H. Huang, R. Yang, Z. Tan, et al., "Quasi-Hodgkin–Huxley Neurons With Leaky Integrate-and-Fire Functions Physically Realized With Memristive Devices," *Advances in Materials* 31, no. 3 (2019): 1803849, https://doi.org/10.1002/adma.201803849.

166. H. Scharstein and J. Math *Biology of Metals* 8 (1979): 403.

167. Z. Xu, A. A. Bernussi, and Z. Fan, "Voltage Pulse Driven VO2 Volatile Resistive Transition Devices as Leaky Integrate-and-Fire Artificial Neurons," *Electronics* 11, no. 4 (2022): 516, https://doi.org/10.3390/electronics11040516.

168. H. J. Caulfield, J. Kinser, and S. K. Rogers, "Optical Neural Networks," *Proceedings of the IEEE* 77, no. 10 (1989): 1573–1583, https://doi.org/10.1109/5.40669.

169. T. Poggio and V. Torre, "A Volterra Representation for Some Neuron Models," *Biological Cybernetics* 27, no. 2 (1977): 113–124, https://doi.org/10.1007/bf00337263.

170. Z. Li, X. Geng, J. Wang, and F. Zhuge, "Emerging Artificial Neuron Devices for Probabilistic Computing," *Frontiers in Neuroscience* 15 (2021): 717947, https://doi.org/10.3389/fnins.2021.717947.

171. H. Liu, Y. Qin, H. Chen, et al., "Artificial Neuronal Devices Based on Emerging Materials: Neuronal Dynamics and Applications," *Advances in Materials* 35, no. 37 (2023): 2205047, https://doi.org/10.1002/adma.202205047.

172. Z. Fan, H. Fan, C. He, and X. Yan *Frontiers of Physics* 20 (2025): 034201.

173. S. Zhang, B. Ma, X. Zhou, et al., "Strain-Controlled Power Devices as Inspired by Human Reflex," *Nature Communications* 11, no. 1 (2020): 326, https://doi.org/10.1038/s41467-019-14234-7.

174. S. Pan, X. Li, J. Bai, et al., "High-Speed and Multi-Level AlScN Ferroelectric Memristor on CMOS-Compatible Tungsten for Electronic Synapses," *Applied Physics Letters* 127, no. 12 (2025): 123505, https://doi.org/10.1063/5.0280404.

175. Z. Wang, J. Zhang, G. Jia, et al., "Self-rectifying Memristors Based on Epitaxial AlScN for Neuromorphic Computing," *Applied Physics Letters* 127, no. 4 (2025): 044105, https://doi.org/10.1063/5.0251575.

176. Z. Ren, Z. Zhang, Y. Zhuge, et al., "Near-Sensor Edge Computing System Enabled by a CMOS Compatible Photonic Integrated Circuit Platform Using Bilayer AlN/Si Waveguides," *Nano-Micro Letters* 17, no. 1 (2025): 261, https://doi.org/10.1007/s40820-025-01743-y.

177. K. Zhu, S. Pazos, F. Aguirre, et al., "Hybrid 2D–CMOS Microchips for Memristive Applications," *Nature* 618, no. 7963 (2023): 57–62, https://doi.org/10.1038/s41586-023-05973-1.

178. S. Yuan, Z. Feng, B. Qiu, et al., "Silicon Carbide Nanowire-Based Multifunctional and Efficient Visual Synaptic Devices for Wireless Transmission and Neural Network Computing," *Science China Materials* 66, no. 8 (2023): 3238–3250, https://doi.org/10.1007/s40843-023-2472-0.

179. Y. Jiang, S. Shi, S. Wang, et al., "In-Sensor Reservoir Computing for Gas Pattern Recognition Using Pt-AlGaN/GaN HEMTs," *Device* (2025): 3, https://doi.org/10.1016/j.device.2024.100550.

180. D. Guo, O. Kapur, P. Dai, et al., "Reservoir Computing Using Back-End-of-Line SiC-Based Memristors," *Materials Advances* 4, no. 21 (2023): 5305–5313, https://doi.org/10.1039/d3ma00141e.

181. Y. Lin, Y. Zhu, F. Wang, et al., "High-Temperature Image Pre-Processing Based on ε-Ga_2O_3 Photo-Synapses," *Advanced Physics Research* 4 (2025): 2400115, https://doi.org/10.1002/apxr.202400115.

182. M. Bu, Y. Wang, Z. Ni, D. Li, D. Yang, and X. Pi, "High-Temperature Optoelectronic Synaptic Devices Based on 4H-SiC," *Science China Information Sciences* 68, no. 4 (2025): 140402, https://doi.org/10.1007/s11432-024-4046-x.

183. W. Shen, P. Wang, G. Wei, et al., "SiC@NiO Core–Shell Nanowire Networks-Based Optoelectronic Synapses for Neuromorphic Computing and Visual Systems at High Temperature," *Small* 20, no. 34 (2024): 2400458, https://doi.org/10.1002/smll.202400458.